electronic reprint

International Tables for Crystallography

Volume H: Powder diffraction

Edited by C. J. Gilmore, J. A. Kaduk and H. Schenk

Chapter 2.4. Electron powder diffraction

J.-M. Zuo, J. L. Lábár, J. Zhang, T. E. Gorelik and U. Kolb

Author(s) of this chapter may load this reprint on their own web site or institutional repository provided that this cover page is retained. Republication of this chapter or its storage in electronic databases other than as specified above is not permitted without prior permission in writing from the IUCr.

International Tables Online is available from it.iucr.org

International Tables for Crystallography (2019). Vol. H, Chapter 2.4, pp. 102–117.

2.4. Electron powder diffraction

J.-M. Zuo, J. L. Lábár, J. Zhang, T. E. Gorelik and U. Kolb

2.4.1. Introduction

Electron powder diffraction is commonly performed in transmission geometry inside a transmission electron microscope using ~80–300 kV high-energy electrons with wavelengths from 0.0418 to 0.0197 Å (Cowley, 1992; Peng *et al.*, 2004). The incident electron beam can be as small as a few nm or as large as tens of µm in diameter. Transmission electron powder diffraction can be obtained from randomly oriented nanocrystalline or amorphous materials. The short electron wavelengths allow the observation of powder diffraction rings over a large range of S (= $\sin\theta/\lambda$). Electron powder diffraction can also be performed using the Bragg reflection geometry in reflection high-energy electron diffraction (RHEED) with 10–30 kV electrons (Ichimiya & Cohen, 2004). RHEED has a limited penetration depth and therefore is mostly used for the study of supported nanoparticles.

Because the electron beam can be formed into a small probe using electromagnetic lenses in a transmission electron microscope, electron diffraction has the advantage of being able to address individual particles in a powder as single crystals. Single-crystal electron diffraction data are often used for the determination of unit-cell parameters (Zuo, 1993; Zuo *et al.*, 1998; Gramm *et al.*, 2006; Sun *et al.*, 2009; Kolb *et al.*, 2006; Zhuang *et al.*, 2011), phase identification (Gramm *et al.*, 2006) or quantitative structural analysis (Vincent & Exelby, 1991; Jansen *et al.*, 1998; Tsuda & Tanaka, 1999; Hovmoller *et al.*, 2002; Sun *et al.*, 2009; Gorelik *et al.*, 2010; Mugnaioli *et al.*, 2012), or in combination with X-ray and neutron powder diffraction for structure determination (Wu *et al.*, 2006; Baerlocher *et al.*, 2007; McCusker & Baerlocher, 2009).

The principle of electron diffraction is similar to that of X-ray diffraction. Both use atomic scattering and interference of the scattered waves to probe the atomic structure. The difference is that electrons are charged particles and interact with both the electrons and nucleus of the atom with a large elastic scattering cross section (several orders of magnitude larger than that of X-rays). The combination of short wavelength, the large scattering cross section and the small electron beam makes electron powder diffraction a powerful technique for the analysis of amorphous or nanocrystalline thin films, nanoparticles and 'small' crystals in general (see Fig. 2.4.1 for an example).

A drawback of the strong interaction of electrons with matter is the presence of multiple-scattering effects. In X-ray diffraction, the measured integrated intensity is often less than predicted by the theory for an ideally imperfect crystal (because of extinction) but larger than predicted by the theory for an ideal perfect crystal. There are two types of extinction: primary and secondary. Primary extinction describes the multiple scattering within a single mosaic block. Primary extinction diminishes the intensity when the mosaic blocks are so large that they behave as fragments of perfect crystals. The effect of electron multiple scattering is similar to primary extinction in X-ray diffraction, except the electron extinction length is short and comparable with the sample thickness. Strong extinction can be an issue when analysis based on kinematical diffraction (single-scattering) theory, as in X-ray powder diffraction, is used for electron diffraction intensities; thus dynamic theory, which takes into account multiple scattering of the incident and diffracted waves inside a crystal, is necessary. Secondary extinction also occurs in electron powder diffraction. However, so far there is no satisfactory treatment of this effect in electron diffraction. For small nanoparticles or nanocrystalline thin films the electron multiple-scattering effects are typically reduced, so quantitative structural information can be extracted from electron powder diffraction using the kinematical approximation (Cockayne & McKenzie, 1988; Ishimaru *et al.*, 2002; Chen & Zuo, 2007; Cockayne, 2007). Recent studies have demonstrated that multiple-scattering effects can be significantly reduced by averaging over a range of crystal orientations using precession electron diffraction (Vincent & Midgley, 1994; Gjonnes *et al.*, 1998; Gemmi *et al.*, 2003; Own *et al.*, 2006; Oleynikov & Hovmoller, 2007). The same benefit is expected in electron powder diffraction with 360° orientation averaging.

The quality of electron powder diffraction work has also benefited from the development of TEM (transmission electron microscopy) technologies. The adoption of field emission guns (FEGs) in conventional transmission electron microscopes led to the development of electron sources with high brightness, small probe size and improved coherence. Electron energy filters, such as the in-column Ω energy filter, allow a reduction of the inelastic background due to plasmon scattering, or higher electron energy losses, with an energy resolution of a few eV (Rose & Krahl, 1995). The development of array detectors, such as charge-coupled device (CCD) cameras or image plates, enables the recording of entire powder diffraction patterns and direct quantification of diffraction intensities over a large dynamic range that was not possible earlier (Zuo, 2000). The latest

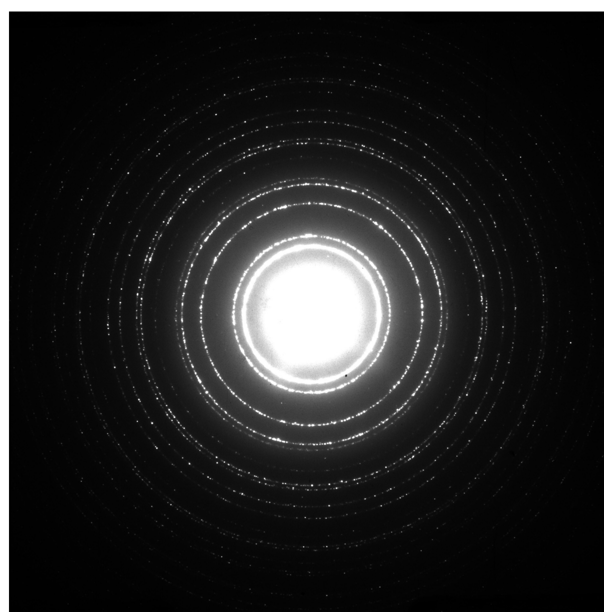

Figure 2.4.1
An electron powder diffraction pattern recorded on an imaging plate from a polycrystalline Al thin film using selected-area electron diffraction geometry with 200 kV electrons.

Copyright © 2019 International Union of Crystallography

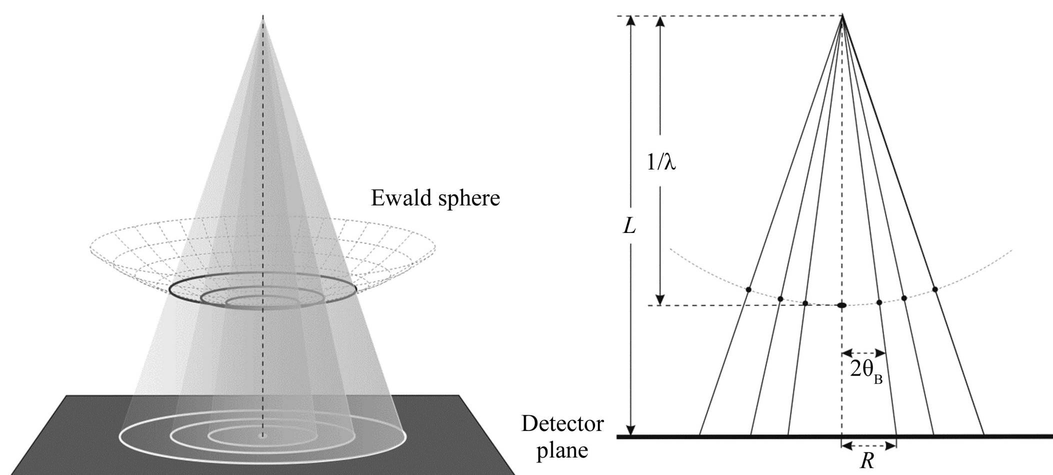

Figure 2.4.2
Schematic diagram of the Ewald sphere construction and the geometry for recording electron diffraction patterns.

development in time-resolved electron diffraction at a time resolution approaching femtoseconds (Elsayedali & Herman, 1990; Siwick *et al.*, 2003) will significantly improve the ability to interrogate structures at high spatial and time resolution.

Irradiation of both organic and inorganic materials with an electron beam can cause severe modification of the structure. The amount of energy deposited into the material can be estimated through the ratio of the elastic and inelastic scattering cross sections. For carbon the ratio for electrons (300 keV) and X-rays (with a wavelength of less than 1 Å) is comparable, meaning that the radiation damage caused by these sources is on the same scale (Henderson, 1995). Electron radiation damage is caused by all kinds of ionization processes, including bond breakdown and subsequent recombination of radicals and active molecular species. Inorganic materials can show knock-on damage (atomic displacement) or sputtering effects (loss of atoms). This damage may lead to a total structural collapse. The collective damage due to electron radiation is quantified using the electron dose and electron dose rates. In many cases the damage can be reduced by minimizing the electron dose received by the sample, cryo-protection, or deposition of a protective conductive layer (Reimer & Kohl, 2008).

This chapter covers the practical issues and theory of electron powder diffraction as well as applications for material analysis. A fundamental description of electron diffraction can be found in *International Tables for Crystallography*, Vol. C (2004) and the book by Zuo & Spence (2017). The present chapter is subdivided into seven sections. Sections 2.4.2 and 2.4.3 cover the theory and the experimental setup of an electron powder diffraction experiment using transmission electron microscopes, respectively. Sections 2.4.4 and 2.4.5 discuss the application of electron powder diffraction data to phase and texture analysis and related techniques. Rietveld refinement with electron powder diffraction data is a relatively new field; this is discussed in Section 2.4.6. The last section reviews pair distribution function (PDF) analysis using electron diffraction data.

2.4.2. Electron powder diffraction pattern geometry and intensity

By J.-M. Zuo and J. L. Lábár

The powder diffraction rings in transmission geometry appear where the cone of diffracted electron beams intersects the Ewald sphere. The intersection creates a ring of diffracted beams, which is then projected onto the planar detector (see Fig. 2.4.2) with a radius (R) according to

$$R = L\tan 2\theta_{\rm B}. \qquad (2.4.1)$$

Here $\theta_{\rm B}$ is the Bragg diffraction angle and L is the camera length.

The d-spacing can be obtained by measuring the length of R in an experimental diffraction pattern using

$$d = \frac{\lambda}{2\sin\theta_{\rm B}}. \qquad (2.4.2)$$

The electron wavelength is determined by the electron accelerating voltage (Φ), in volts:

$$\lambda = \frac{h}{(2m_e\Phi)^{1/2}} \simeq \frac{1.226}{[\Phi(1+0.97845\times10^{-6}\Phi)]^{1/2}}. \qquad (2.4.3)$$

The wavelength of high-energy electrons is relatively short. For 200 kV electrons, the wavelength is 0.025 Å and the Bragg angle is very small. For example, for d = 2.5 Å the electron scattering angle θ is 5 mrad. For a small Bragg angle one can use the approximation $\sin\theta \simeq \tan\theta \simeq \theta$. This gives the relationship

$$d \simeq \frac{L\lambda}{Rd}. \qquad (2.4.4)$$

At large scattering angles with $\sin\theta/\lambda$ 2 Å^{-1} or greater, a better approximation is given by (Cowley & Hewat, 2004)

$$d \simeq \frac{L\lambda}{R}\left(1+\frac{3R^2}{8L^2}\right). \qquad (2.4.5)$$

The camera length L can be determined using a sample with known d-spacings, while the electron wavelength or acceleration voltage can be calibrated using high-order Laue zone (HOLZ) lines in convergent-beam electron diffraction (CBED) patterns (Zuo, 1993).

For a small parallelepiped crystal fully illuminated by a coherent electron beam of intensity I_0, the kinematic diffraction intensity is given by

$$I_{\rm SC} = I_0\frac{|F_{hkl}|^2}{L^2}\left\{\frac{\sin[\pi\mathbf{S}_{hkl}\cdot N_1\mathbf{a}]}{\sin[\pi\mathbf{S}_{hkl}\cdot\mathbf{a}]}\,\frac{\sin[\pi\mathbf{S}_{hkl}\cdot N_2\mathbf{b}]}{\sin[\pi\mathbf{S}_{hkl}\cdot\mathbf{b}]}\,\frac{\sin[\pi\mathbf{S}_{hkl}\cdot N_3\mathbf{c}]}{\sin[\pi\mathbf{S}_{hkl}\cdot\mathbf{c}]}\right\}^2, \qquad (2.4.6)$$

where N_1, N_2 and N_3 are the number of unit cells along the three axis directions, and F_{hkl} is the electron structure factor of the hkl reflection:

$$F_{hkl} = \sum_{i=1}^{n} f_i^e T_i \exp[2\pi i(hx_i + ky_i + lz_i)]. \qquad (2.4.7)$$

Here T is the atomic displacement factor, which accounts for atomic thermal vibrations, and the electron atomic scattering factor f_i^e is defined by equation (4.3.1.13) in *International Tables for Crystallography*, Vol. C (2004). For a reflection with the scattering vector $\mathbf{g}_{hkl}$ the deviation from the Bragg condition of the hkl reflection is expressed by the excitation error $\mathbf{S}_{hkl}$:

$$\mathbf{k} - \mathbf{k}_0 = \mathbf{g}_{hkl} + \mathbf{S}_{hkl}. \qquad (2.4.8)$$

The diffraction intensity recorded in a powder diffraction pattern is the integrated intensity over the crystal orientation and the detector area. A change in crystal orientation leads to a change in the excitation error normal to the diffracted beam in the plane of Bragg reflection. The integration in these three directions is equivalent to integration over the reciprocal-space volume around the Bragg peak. The result gives the diffraction power of a sample with a large number of crystallites for the hkl reflection as (Warren, 1990)

$$P_{hkl} = I_0 \frac{\lambda^2 m_{hkl} V_{\rm sample} d_{hkl}}{2V_c^2} \left|F_{hkl}\right|^2, \qquad (2.4.9)$$

where $V_{\rm sample}$ is the sample volume, m_{hkl} is the multiplicity of the reflection based on the symmetry-equivalent number of hkl reflections, and V_c is the volume of the unit cell. For randomly oriented powder samples, the diffraction power is uniformly distributed over the bottom edge of a cone of half apex angle $2\theta_{hkl}$ and height L, and the peak intensity is more appropriately described by the power per unit length of the diffraction circle (Vainshtein, 1964):

$$I_k = \frac{P_{hkl}}{2\pi L \sin 2\theta_{hkl}} = \frac{I_0}{4\pi L} \frac{\lambda d_{hkl}^2 m_{hkl} V_{\rm sample}}{V_c^2 \cos\theta_{hkl}} \left|F_{hkl}\right|^2. \qquad (2.4.10)$$

Here $\cos\theta_{hkl} \simeq 1$ is a good approximation for electron diffraction and this formula is presented in equation (2.4.1.3) in *International Tables for Crystallography*, Vol. C (2004).

The kinematic approximation in electron diffraction is valid only for very small crystals. Defining the validity of the kinematic approximation for different crystals has been difficult and the subject of extensive debate (Blackman, 1939; Vainshtein, 1964; Turner & Cowley, 1969; Cowley, 1995). For single-crystal electron diffraction, numerous studies using CBED have demonstrated an almost perfect fit to experimental diffraction intensities using dynamic theory. Using this fitting approach, experimental structure-factor amplitudes and phases can be measured through a refinement process with high accuracy (Saunders *et al.*, 1995; Tsuda *et al.*, 2002; Zuo, 2004). However, this approach requires knowledge of the approximate crystal structure and can rarely be used for powder electron diffraction, where unknown crystal structures are often studied. In developing a theory for the integrated intensity for powder electron diffraction, the magnitude of the dynamic effect and its dependence on crystal orientations, defects, thickness variations and crystal shape must be considered. In X-ray and neutron diffraction, the combination of these factors led to the highly successful kinematical theory of ideal imperfect crystals with randomly distributed mosaic blocks. For electron diffraction, an all-encompassing theory of integrated intensity has been elusive because of the small electron coherence length, which is much less than the size of typical mosaic blocks detected by X-ray and neutron diffraction, and strong scattering. An approximation has been developed to take account of dynamical scattering using the two-beam theory (Blackman, 1939). Under this approximation, the integrated dynamic intensity I_d over a large range of excitation is given by the expression

$$I_d \propto \left|F_{hkl}\right| \int_0^{A_{hkl}} J_0(2x)\,{\rm d}x. \qquad (2.4.11)$$

Here

$$A_{hkl} = \frac{\lambda\gamma\left|F_{hkl}\right|t}{V_c \cos\theta_{hkl}} \simeq \frac{\lambda\gamma\left|F_{hkl}\right|t}{V_c}, \qquad (2.4.12)$$

where t is the thickness of the crystallite along the electron-beam direction, γ is the relativistic constant of electrons and $J_0(2x)$ is the zero-order Bessel function. For a very small value of A_{hkl} the Bessel function $J_0(2x)$ is nearly constant with a value of 1 and the diffraction intensity approaches that of the kinematical limit. From this, the following formula can be derived for the dynamical intensity:

$$I_d = \frac{I_0}{4\pi L} \frac{d_{hkl}^2 m_{hkl} V_{\rm sample}}{V_c \gamma t} \left|F_{hkl}\right| \int_0^{A_{hkl}} J_0(2x)\,{\rm d}x. \qquad (2.4.13)$$

For very large A_{hkl}, the integral over the Bessel function approaches the value of 1/2 and in this case the diffraction intensity is proportional to the structure-factor amplitude instead of its square as predicted by kinematical theory.

The extent of dynamic effects that can be reduced by averaging over crystal orientations has been demonstrated by precession electron diffraction (PED). This technique was originally developed by Vincent & Midgley (1994) to improve the single-crystal electron diffraction intensities for structural analysis. In PED, the incident electron beam is tilted and precessed along a conical surface that is centred on the electron optical axis. Below the crystal, the diffraction pattern is tilted back with the position of the direct beam remaining approximately constant during precession. The diffraction pattern then generally appears similar to a conventional electron diffraction pattern. The measured diffraction intensity, however, is a double integration over the two-dimensional detector and the incident-beam angles defined by the precession cone surface. Experimental and theoretical studies of PED integrated intensities have shown an overall 'more kinematical' behaviour with less sensitivity to crystal thickness and exact orientation than for conventional electron diffraction patterns. Simulations also showed that the dynamical effects are still present in the PED integrated intensities, but the extent of the dynamic effect as measured by the correlation between the integrated intensity and the squared amplitude of the structure factor follows the empirical rules:

(i) The correlation increases with the precession angle.
(ii) The correlation is more pronounced for higher-order reflections than lower-order ones, for which the integration over the different excitation error is less complete.
(iii) The correlation also improves as the crystal thickness decreases.

In the electron powder diffraction of randomly oriented crystals, the angular integration is performed over the entire solid angle. Zone-axis patterns with enhanced dynamical interaction between the diffracted beams are also included in this solid angle. However, the overall probability for a crystal to be in exact zone-axis orientation is very small, even if the zone axis is defined

within a wedge of tens of milliradians. Thus, powder electron data generally tend to be more kinematical than single-crystal data.

2.4.3. Electron powder diffraction techniques

By J.-M. Zuo and J. Zhang

The basic setup for electron powder diffraction uses a transmission electron microscope equipped with an area electron detector (photographic film, CCD camera *etc.*). Thin films, such as amorphous carbon or holey carbon films supported on metal grids, are typically used to support powder samples, which are then mounted and inserted into the transmission electron microscope inside a TEM sample holder. Solid free-standing thin films can be placed directly on top of a metal grid.

The electron beam used for a powder electron diffraction experiment is shaped using electromagnetic lenses. A modern transmission electron microscope uses at least three sets of magnetic lenses for the illumination system: condensers I and II, and the objective prefield. The prefield is part of the objective lens system before the sample acting as a lens. Some transmission electron microscopes come with an additional condenser lens (condenser III, or condenser mini-lens), which can be used for nanodiffraction. These lenses are used in various combinations to set up electron illumination for selected-area electron diffraction (SAED) or nano-area electron diffraction (NAED) (Zuo, 2004). The major difference between these two is the area of illumination, which is controlled by the strength (or focal length) of the condensers II and III.

An issue to be considered during setup of the electron beam for powder diffraction is the electron lateral coherence length. In a transmission electron microscope, the electron coherence is defined by the coherence length seen at the condenser aperture. According to the Zernike–Van Cittert theorem, the degree of coherence between electron wavefunctions at two different points far away from a monochromatic electron source is given by the Fourier transform of the source intensity distribution (Cowley, 1999). If we assume that the source has a uniform intensity within a circular disc, the coherence function is then given by $\lambda J_1(\pi\beta r/\lambda)/\beta r$ with J_1 being the first-order Bessel function, r the radial distance at the aperture and β the angle sustained by the electron source. The lateral coherence length L, which is often referred to in the literature, is defined by r at the first zero of J_1, which has the value of $L = 1.2\lambda/\beta$. The source seen by the condenser aperture inside a transmission electron microscope is the source image formed after the condenser-I lens. For a Schottky emission source, the emission diameter is between 20 and 30 nm according to Botton (2007). For a condenser aperture placed 10 cm away from the electron source image, a factor of 10 source demagnification provides a coherence length from 100 to 150 µm. When a smaller condenser aperture is used, such as in NAED, the electron beam can be considered as approximately coherent and the lateral coherence length on the same is limited by the beam convergence angle α with $L_{\rm sample} = 1.2\lambda/\alpha$.

2.4.3.1. *Selected-area electron diffraction (SAED)*

SAED is formed using the transmission electron microscope illumination, which is spread out over a large area of the specimen to minimize the beam convergence angle. The diffraction pattern is first formed at the back focal plane of the objective lens and then magnified by the intermediate and projector lenses (only one is shown) onto the screen or electron detector (Fig. 2.4.3). The recorded diffraction pattern is from an area of interest selected by placing an aperture in the conjugate (imaging) plane of the objective lens. Only electron beams passing through this aperture contribute to the diffraction pattern. For a perfect lens without aberrations, electron beams recorded in the diffraction pattern come from an area that is defined by the image of the selected-area aperture at the specimen plane. The aperture image is demagnified by the objective lens. In a conventional electron microscope, rays at an angle to the optic axis are displaced away from the centre because of the spherical aberration of the objective lens (C_s) as shown in Fig. 2.4.3. The displacement is proportional to $C_s\alpha^3$, where α is twice the Bragg angle. The smallest area that can be selected in SAED is thus limited by the objective lens aberrations. This limitation is removed by using an electron microscope equipped with a transmission electron microscope aberration corrector placed after the objective lens (Haider *et al.*, 1998).

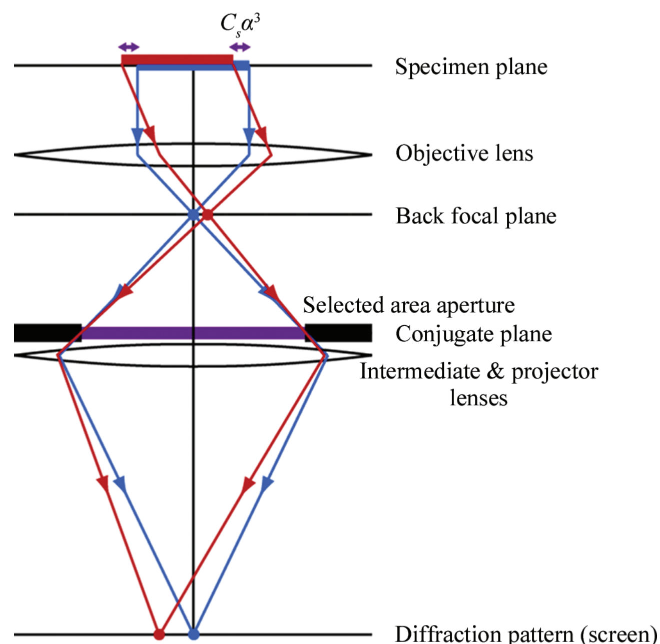

Figure 2.4.3
Schematic illustration of selected-area electron diffraction in conventional TEM. (Provided by Jun Yamasaki of Nagoya University, Japan.)

The major feature of SAED is that it provides a large illumination area, which is beneficial for recording diffraction patterns from polycrystalline samples as it leads to averaging over a large volume (for example, a large number of nanoparticles). SAED can also be used for low-dose electron diffraction, which is required for studying radiation-sensitive materials such as organic thin films.

2.4.3.2. *Nano-area electron diffraction (NAED)*

NAED uses a small (nanometre-sized) parallel illumination with the condenser/objective setup shown in Fig. 2.4.4 (Zuo *et al.*, 2004). The small beam is achieved by reducing the convergence angle of the condenser-II crossover and placing it at the focal plane of the objective prefield, which then forms a parallel-beam illumination on the sample for an ideal lens. A third condenser lens, or a mini-lens, is required for the formation of a nanometre-sized parallel beam. For a condenser aperture of 10 µm in diameter, the probe diameter is ~50 nm with an overall magnification factor of 1/200 in the JEOL 2010 electron microscopes (JEOL, USA). The smallest beam convergence angle in NAED is

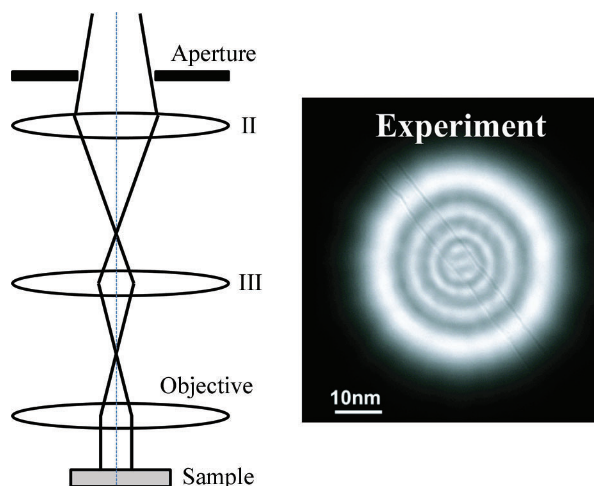

Figure 2.4.4
Schematic illustration of electron nanoprobe formation using a combination of condenser lenses (II and III) and the objective lens. The beam divergence angle is kept at a minimum by forming a crossover at the front focal plane of the objective lens. An image of an experimental electron nanoprobe is shown on the right with a carbon nanotube contained inside the probe.

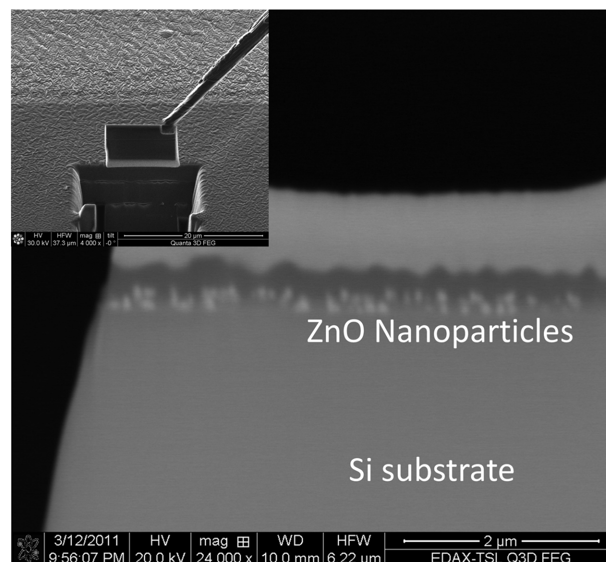

Figure 2.4.5
Sample preparation and lift-out using a focused ion beam (FIB). A thin section of the sample is cut out using the FIB and attached to a mechanical probe for lift-out (inset). The image shows the lift-out section containing ZnO nanoparticles in bright dot-like contrast supported on an Si substrate.

limited by the aberrations of the illumination lenses. A beam convergence angle as small as ~0.05 mrad has been reported (Zuo *et al.*, 2004). A diffraction pattern recorded using NAED is similar to one recorded by SAED. The major difference is that the diffraction volume is defined directly by the electron probe in NAED. Since all electrons illuminating the sample are recorded in the diffraction pattern, NAED in an FEG microscope also provides higher beam intensity than SAED (the probe current intensity using a 10 μm condenser-II aperture in a JEOL 2010F is $\sim 10^5$ e s^{-1} nm^{-2}) (Zuo *et al.*, 2004).

The small probe size is most useful for studying a small section of thin films or for selection of nanoparticles for powder diffraction. The small beam size reduces the background in the electron diffraction pattern from the surrounding materials.

2.4.3.3. *Sample preparation*

The success of an electron powder diffraction experiment to a large extent depends on sample preparation. The powder sample has to be suitable for electron-beam observation, and the sample also needs to be compatible with the vacuum environment of the microscope. *In situ* experiments can be carried out using special holders for cooling, heating and cryogenic or environmental transfer. Special microscopes are also available to provide a gaseous or ultra high vacuum environment for the investigation of structures under a gas or at ultra low pressure, or *in situ* sample preparation.

The observed area of the sample must be electron transparent, *i.e.* have a thickness of less than or comparable to the inelastic mean free path of electrons. The inelastic mean free path increases with the electron voltage (Egerton, 2011). The typical sample thickness ranges from a few tens to hundreds of nanometres for 200 kV high-energy electrons (see Table F.1 in Zuo & Spence, 2017).

The sample-preparation techniques can be divided into three categories: (i) bulk-based for bulky materials and supported thin films, (ii) powder-based techniques and (iii) free-standing thin films over a supporting grid prepared by vacuum evaporation or sputtering.

The bulk-based techniques involve mechanical cutting, thinning/polishing and perforation. An ion beam is typically used in the last step of perforation to create a thin area around the edge of a hole for electron-beam observation. Chemical and electrolytic methods are also often used for preparing electron-transparent samples. While these methods have been applied to a broad range of materials, they are mostly used for metals or semiconductors to create smooth sample surfaces free from defects or sample heating caused by ion-beam irradiation. Mechanical thinning and polishing are sometimes done with a wedge angle with the help of a tripod. The thin region next to the edge only requires a brief ion-beam bombardment to make it electron transparent. A detailed description of traditional sample-preparation techniques for TEM can be found in Barna & Pécz (1997). The above techniques are applicable to both thin films and bulk nanocrystalline materials. The powder-based techniques use dispersion of powders on thin supporting films placed on metal grids specially made for TEM observations. This technique is most suitable for nanoparticles. For micron or larger-sized powders, additional grinding is used to produce smaller particles. The most commonly used supporting films are continuous amorphous carbon films, holey carbon films, networked carbon fibres (lacey carbon), amorphous silicon nitride and SiO_x. For amorphous carbon films, an ultra thin version is available which is especially useful for nanoparticle samples.

A recent development in TEM sample preparation is the use of a focused ion beam of Ga^+ ions for cross-sectioning a sample. The focused ion beam can drill a precise hole in the sample. The same ion beam can also be scanned over a sample surface to form an image by collecting the secondary electrons or ions generated by the beam. The ion column can be integrated into an electron column in a scanning electron microscope in the so-called dual-beam configuration. An image can be formed using either electrons or ions. Most often the electron beam is used for sample inspection, while the ion beam is used for patterning and milling. This allows precise control over the position and thickness of the cross section, which is very practical for characterization of

semiconductor devices or failure analysis in general (Fig. 2.4.5). Further details about ion-beam techniques can be found in Lábár & Egerton (1999) and Orloff *et al.* (2002). For a comprehensive review of sample-preparation techniques for TEM, see Őzdöl *et al.* (2012).

2.4.3.4. *Diffraction data collection, processing and calibration*

Experimental electron powder diffraction data are collected using two-dimensional area electron detectors. Experimental issues involved in the diffraction-pattern recording procedure are electron optical alignment, diffraction-pattern collection and calibration, with particular care taken in adjusting the specimen height position (eucentric position), selection of a suitable illumination-beam convergence angle and diffraction-camera length, and finally projector-lens focusing. The diffraction-camera length is determined by the setting of intermediate and projector lenses in combination with the objective lens. To calibrate the diffraction-camera length, a standard sample is placed in the eucentric position of the objective lens at the standard focus. At this setting, the specimen plane is conjugate to the selected-area aperture (Fig. 2.4.3) and the sample image appears in focus. To obtain a sharp diffraction pattern, the detector plane must be conjugate to the back focal plane of the objective lens. This can be achieved by setting up a parallel-beam illumination and adjusting the intermediate-lens focus length to bring the direct beam into a sharp focus.

Currently available area electron detectors are CCD and CMOS cameras, imaging plates (IPs) and photographic film. While photographic film has a long history of use in electron microscopy, its limited dynamic range makes it less useful for electron diffraction data collection. Both CCD cameras and IPs are digital recorders capable of collecting electron intensity over a large dynamic range. The crucial characteristics of digital recording systems are the gain (g), linearity, resolution, detector quantum efficiency (DQE) and the dynamic range. The gain of a CCD or CMOS camera can be normalized using a flat-field illumination; the gain in IPs is assumed to be constant. The detector resolution is characterized by the point-spread function (PSF), which is roughly the detector's response to a point-like illumination. These characteristics for CCDs and IPs have been compared by Zuo (2000). The intensity of an electron diffraction pattern recorded with a digital detector is given by

$$I^{\rm recorded}(i,j)=g(i,j)H(i,j)\otimes I^{\rm original}(i,j)+n(i,j), \qquad (2.4.14)$$

where $g(i, j)$ is the detector gain image, H is the PSF of the detector, n is the detector noise and $I^{\rm original}$ is the intensity of scattered electron beams originally received by the detector. The i and j are the pixel coordinates of the detector. The PSF is experimentally characterized and measured by the amplitude of its Fourier transform, or the so-called modulated transfer function (MTF). The effects of the PSF can be removed by deconvolution. The Richardson–Lucy method is specifically targeted for Poisson processes, which can be applied to CCD images (Zuo, 2000). The alternative to the removal of the PSF is to treat it as part of the peak broadening that can be used to fit the powder pattern.

The noise in the experimental data is characterized by the DQE:

$$\mathrm{var}(I)=\frac{m\bar{g}I}{\mathrm{DQE}(I)}. \qquad (2.4.15)$$

Here I is the experimentally measured intensity, var stands for the variance, m is the area under the MTF and $\bar{g}$ is the average gain of the detector. Once the DQE is known, this expression allows an estimation of the variance in measured intensity, which is essential for quantitative intensity analysis where the variance is often used as the weight for comparing experimental and fitted data.

The performances of CCDs and IPs for electron diffraction pattern recording are different at different electron dose rates. At low dose rates, the DQE of the CCD camera is limited by the readout noise and the dark current of the CCD. IPs have better performance in the low dose range due to the low dark current and low readout noise of the photomultipliers used in IP readers. At medium and high dose rates, the IP signal is affected mostly by the linear noise due to the granular variation in the phosphor and instability in the readout system, while for CCDs the noise is mostly linear noise in the gain image.

Electromagnetic lenses are not perfect and have aberrations affecting the collected data. In most transmission electron microscopes, electron diffraction patterns are produced using the post-specimen magnetic lenses. For electron diffraction, the most important aberration is the distortion of the projector lens, causing a shift of an image point. There is no blurring in diffraction patterns associated with the lens distortion. However, the distortion affects the overall shape of diffraction patterns. The distortion is most obvious at low camera lengths, where the pattern may seem stretched or twisted at high scattering angles. There are three types of distortion of the same order as the spherical aberration of the lens. They are called pin-cushion, barrel and spiral distortions (Reimer, 1984). A distortion can also arise from the use of an electron energy filter, where a lower order of distortion can be introduced with the use of non-spherical lenses (Rose & Krahl, 1995).

For quantitative analysis an electron powder diffraction pattern recorded on an area detector needs to be integrated into one-dimensional powder diffraction data (Fig. 2.4.6). The integration involves four separate steps: (i) identifying areas of the diffraction pattern for integration, (ii) centring the diffraction pattern, (iii) applying a diffraction pattern distortion correction, if there is any, and (iv) integrating intensities for a constant diffraction angle. Electron powder diffraction patterns can be recorded on a crystalline support film, which gives sharp diffraction spots distinct from the powder diffraction rings. The sharp diffraction patterns from the support film can be excluded from the powder diffraction intensity integration in step (i) by using a mask. The same approach can be used to eliminate any alien features from a diffraction pattern caused, for instance, by the aperture or the energy filter. The diffraction pattern centring is based on the analysis of the transmitted beam in the centre of the pattern. As the transmitted beam is usually very strong and is often overexposed, finding its centre may be a non-trivial task. In order to prevent detector damage in the area of the transmitted beam a beam stop is often used. In this case, the central area in the pattern may have an irregular shape not suitable for the centring procedure. Non-distorted diffraction patterns can be centred by finding the centre of the concentric diffraction rings either by locating the position of the maximum diffraction peak intensity along the ring and using these positions to determine the centre of the ring, or by searching for the centre that gives the maximum correlation between $I(g)$ and $I(-g)$. For distorted diffraction patterns, the centring and the distortion correction must be carried out simultaneously.

The distortion correction requires a powder sample with known d-spacings. The amount of distortion can be obtained by

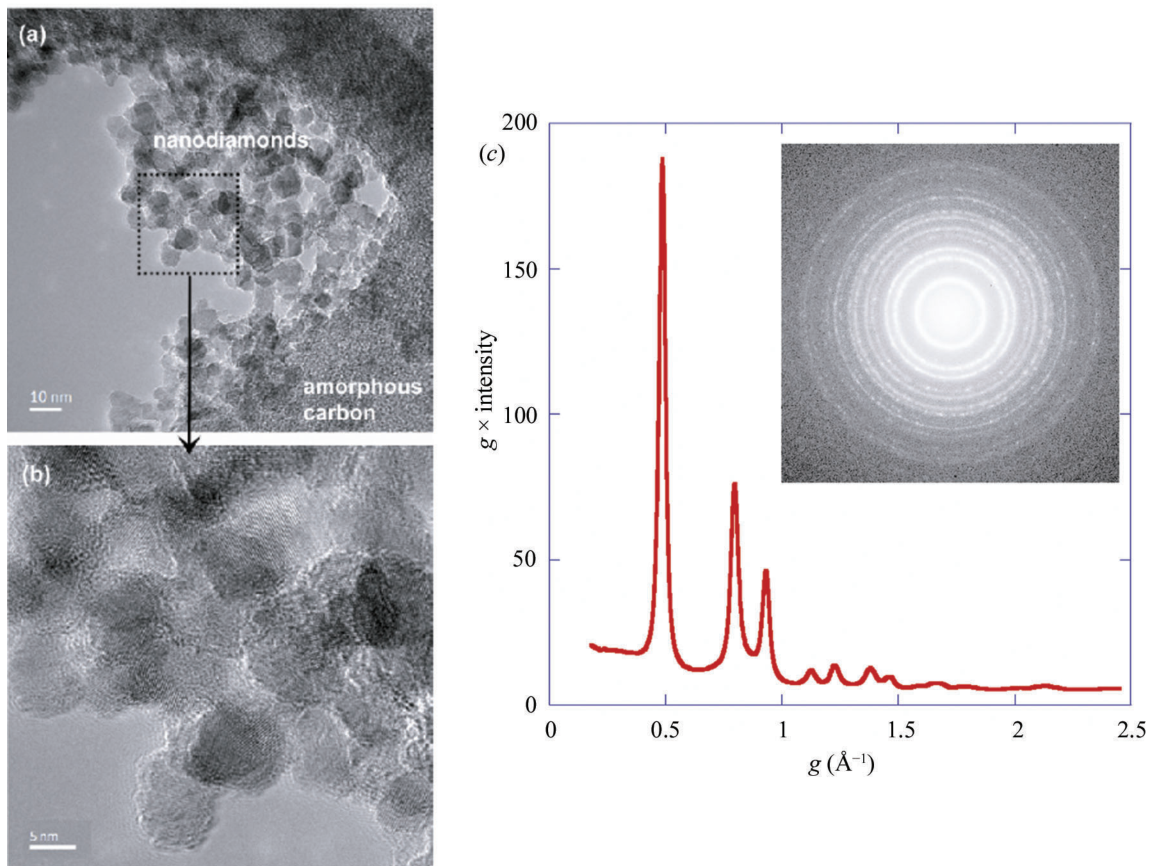

Figure 2.4.6
An example of electron powder diffraction recording for nanodiamonds. (*a*) A TEM image showing nanodiamond particles supported on amorphous carbon, (*b*) the magnified image from the boxed region of (*a*), and (*c*) the recorded electron powder diffraction pattern from nanodiamond particles and the obtained radial intensity profile.

fitting the diffraction ring position $R_d(\varphi)$ using a cosine expansion with

$$R_d(\varphi) = R + \sum_{n=1}^{N} \Delta R_n \cos n(\varphi - \varphi_n), \qquad (2.4.16)$$

where R is the average radius (zero order) of the diffraction ring, ΔR represents the amplitude of distortion of order n and φ is the azimuthal angle. Once the distortion is calibrated and excluded from the data, the diffraction intensity integration can be simply carried out by summing the recorded diffraction intensity according to the radius using

$$I_n = \frac{1}{N} \sum I[i, j], \qquad (2.4.17)$$

where the sum is taken over $R(i, j, i_0, j_0, \Delta R) \in \{n\delta, (n+1)\delta\}$. Here the powder diffraction intensity is integrated in fine discrete steps along the radius of a diffraction pattern (corresponding to increasing scattering angle) with an interval of δ, the summation is done over all diffraction pixels that fall between the radius of $n\delta$ and $(n + 1)\delta$ and N is the number of these pixels.

Filtering the inelastic background is an option for electron microscopes equipped with an electron energy filter. A major contribution to the inelastic background in electron diffraction patterns comes from bulk plasmon excitation (Egerton, 2011). This can be filtered out by dispersing the electrons according to their energies using magnetic or electrostatic fields inside an electron energy filter and using a slit of a few eV in width around the elastic (zero-loss) electron beam. For use with an area electron detector for electron diffraction, the filter must also have a double focusing capability to function as an imaging lens. There are two types of electron imaging energy filters that are currently employed: one is the in-column Ω energy filter and the other is the post-column Gatan imaging filter (GIF). The in-column Ω filter is placed between the transmission electron microscope's intermediate and projector lenses and can be used in combination with IPs, as well as with a CCD or CMOS camera. The GIF is placed after the projector lens and the use of a GIF for electron diffraction typically requires the transmission electron microscope to be switched to a special low-camera-length setting. For electron diffraction, geometric distortions, isochromaticity and the angular acceptance are important characteristics of the imaging filter (Rose & Krahl, 1995). Geometrical distortions arise from the use of non-cylindrical lenses inside the energy filter. The distortion can be caused by optical misalignment, which is an issue with the GIF with its low camera-length setting. The amount of distortion can be measured using a standard calibration sample and corrected using numerical methods. Isochromaticity defines the range of electron energies for each detector position. Ideally, this should be the same across the whole detector area. The angular acceptance defines the maximum range of diffraction angles that can be recorded on the detector without a significant loss of isochromaticity (Rose & Krahl, 1995).

2.4.4. Phase identification and phase analysis

By J. L. Lábár

For known structures, powder diffraction patterns can be used for identification of the crystalline phases and quantification of their

volume fraction for samples containing multiple phases. These procedures are usually performed in two steps. First, the candidate phases must be selected to produce a shortlist of the structures that may be present in the sample. Preparation of the shortlist generally relies on *a priori* chemical information [obtained *e.g.* from energy-dispersive X-ray spectroscopy (EDS) or electron energy-loss spectrometry (EELS)] to reduce the number of candidate phases (crystalline structures) that are searched for (Lábár & Adamik, 2001; Lábár, 2006) in a comprehensive database such as the Powder Diffraction File (Faber & Fawcett, 2002). The identification of the crystalline phases in the experimental data is done through pattern fingerprinting. Final confirmation of phase identification is provided by the success of quantitative or semi-quantitative phase analysis, which determines the phase fractions and amount of texture.

In principle, the Le Bail structure-factor extraction (decomposition) method (see Chapter 3.5) could also be used for electron diffraction ring patterns from nanocrystals that are small enough to scatter kinematically or quasi-kinematically (Moeck & Fraundorf, 2007). The main advantage of this approach would be that no assumptions about the structure have to be made. However, none of the methods available for electron diffraction data follow this approach and identification of crystalline phases generally follows a different route [qualitative phase analysis (Lábár & Adamik, 2001) or traditional structural fingerprinting (Moeck & Rouvimov, 2010)].

After a two-dimensional ring pattern is integrated into a one-dimensional intensity distribution, the positions and intensities of peaks are extracted. The positions of the diffraction peaks are used as minimum information for fingerprinting. For successful phase identification the largest d values (at the smallest scattering angles) are crucial. Unfortunately, they are not always listed in the X-ray diffraction databases (Moeck & Fraundorf, 2007). Use of diffraction-peak intensities for fingerprinting has limited validity due to the deviation of electron diffraction intensities from the kinematic scattering formalism and the possible presence of texture in the sample. Phase analysis (fingerprinting) is complete when only one (set of) model structure(s) remains (out of several candidates listed in the previous step) on the basis of best fit between the model and the measured diffraction patterns. The addition of features to the Powder Diffraction File to make it more useful for phase identification using electron diffraction data is an active area of development.

Once a structural model is selected, the quantitative fit of diffraction intensities is performed. The quantitative modelling requires knowledge of the atomic positions within the unit cell. Atomic coordinates are not listed in the older PDF-2 database, but are given for many phases in the PDF-4+ database that combines five collections provided by different institutions. There are also open databases, like COD (http://www.crystallography.net/cod/), NIMS_MatNavi (http://crystdb.nims.go.jp/index_en.html) or AMCDS (http://rruff.geo.arizona.edu/AMS/periodictable.php). They also list atomic coordinates and can export structure data as CIF files.

For calculation of the electron structure factors, the electron atomic scattering factors are given in *International Tables for Crystallography*, Vol. C (2004). In the case of kinematical scattering, the intensity is proportional to the square of the electron structure factor F_{hkl}. If necessary, an absorption correction can be performed using the Weickenmeier & Kohl (1991) formalism.

Application of the quasi-kinematic formalism paves the way to giving an estimate of grain size in the beam direction (Lábár *et al.*, 2012). However, there is no straightforward correlation of this value with the actual crystal size or the thickness of the TEM sample. The grain size coming from the quasi-kinematic formula is also different from the size of the coherently scattering domains that could be determined from the broadening of the diffraction peaks (Ungár *et al.*, 2001), which is related to the lateral size of the crystallites (grains, particles) in the TEM sample.

In addition to peak positions and intensities, the peak shape and the background intensity have to be fitted. The pseudo-Voigt peak shape is most frequently used in electron diffraction phase analysis. The background intensity distribution in powder electron diffraction patterns is modelled empirically. The width of the diffraction peaks is an empirical parameter in the present implementation of phase analysis (Lábár, 2009). A Williamson–Hall type analysis of the variation of the experimentally observed peak width with the diffraction vector is also possible for simple profiles with well separated peaks (Gammer *et al.*, 2010); however, so far it has only been done for single-phase diffraction profiles with a known material without an attempt to combine it with phase analysis. Making the peak width dependent on grain size and defect structure (Ungár *et al.*, 2001) would in principle also be possible for phase analysis from powder electron diffraction data, but has not been implemented so far.

Selection of the appropriate structure model is done based on the value of the goodness-of-fit (GOF) criterion. For a one-dimensional electron diffraction profile recorded for n pixels, the GOF is given by

$$\mathrm{GOF} = \frac{1}{n-p} \sum_{k=n_0}^{n} \frac{1}{w_k} (I_k^{\mathrm{exp}} - I_k^{\mathrm{calc}})^2, \qquad (2.4.18)$$

where p is the number of parameters used in fitting, w_k is a relative weight of the intensity value at the kth pixel, and I_k^{exp} and I_k^{calc} are the experimentally measured and calculated intensity values for the kth pixel, respectively.

Structure models are described in parametric form (including experimental parameters, peak-shape parameters together with volume fractions of the phases and their fibre-textured components: p parameters altogether) and the p-dimensional parameter space is explored to calculate the GOF. The model with the smallest GOF is accepted. In phase analysis the best match is searched for by using the downhill simplex algorithm (Nelder & Mead, 1965). The semi-global simplex was found to be robust and allowed easy escape from local minima (Zuo & Spence, 1991) when used for fitting CBED patterns.

For polyphasic diffraction profiles, the volume fraction of phases is calculated at the end of the fitting procedure. It is assumed that the net diffraction intensity in each pixel is a linear combination of contributions of the individual phases (random and textured fractions are treated as independent model components). The over-determined set of equations is solved using least-squares minimization. The number of equations is reduced, while keeping the information content of all equations, by forming matrix $\mathbf{A}$ as

$$a_{i,j} = \sum_k \mathrm{Model}_k(i)\mathrm{Model}_k(j), \qquad (2.4.19)$$

where summation is performed for all pixels k for the model functions of the ith and jth phases, and vector $\mathbf{b}$ as

$$b_i = \sum_k (\mathrm{Measured}_k - \mathrm{Background}_k)\mathrm{Model}_k(i). \qquad (2.4.20)$$

The coefficients of the linear combination are obtained by solving for vector $\mathbf{x}$ the matrix equation $\mathbf{Ax} = \mathbf{b}$ using matrix inversion.

The coefficients of this linear combination [$x(i)$] put the intensities of the peaks in phase i on the absolute scale. $I_{\max}(i)$, the intensity calculated on the absolute scale for the strongest (100%) diffraction peak of phase i, gives the intensity diffracted by one unit cell (structure factors are calculated for the atoms of one unit cell). Then $x(i)/I_{\max}(i)$ is the number of unit cells of phase i in the analysed volume. Consequently, the volume extended by phase i in the analysed volume is $V(i)x(i)/I_{\max}(i)$, where $V(i)$ is the volume of the unit cell of phase i. The volume fraction of phase f_i is then given by

$$f_i = \frac{V(i)x(i)}{I_{\max}(i)} \bigg/ \sum_i \frac{V(i)x(i)}{I_{\max}(i)}. \qquad (2.4.21)$$

In addition to volume fractions of phases and their fibre-textured components, the same method can determine the variation (contraction, dilation, distortions) of the unit cell, provided experimental parameters specific to electron diffraction (*e.g.* the camera length and pattern distortion) are properly calibrated. The reliability of the camera-length calibration (systematic error) is usually around 2% (Williams & Carter, 2009); in the best cases accuracy of better than 0.3% has been reported (Lábár *et al.*, 2012). Consequently, only large variations in the lattice parameter can be determined reliably from powder electron diffraction data and the typical accuracy of powder X-ray diffraction cannot be attained.

There are two main advantages of phase analysis from powders by electron diffraction compared with X-ray diffraction. First, much smaller volumes can be studied. Diffraction information can be collected from thin layers of a few tens of nanometres thickness, enabling precise identification of the inspected volume. If needed, different lateral sections from different depths of a bulk sample can be studied by TEM, thus providing three-dimensional information about the sample. In a non-homogeneous sample, electron diffraction data can be collected from different areas, allowing detection of different phases or texture components at a spatial resolution and sensitivity superior to X-ray diffraction methods (Lábár *et al.*, 2012).

The accuracy of the phase-content identification in a mixture for the major components is around 10–15% (Lábár *et al.*, 2012). The detection limit depends on the scattering power of the component. A weakly scattering phase of Cr in a strongly scattering matrix of Ag could only be detected at the content of 2%, while the presence of 5% Ag in a relatively weakly scattering Ni matrix allowed full quantification of the two phases (Lábár *et al.*, 2012). Thus, generally 5% (by volume) is accepted as the detection limit for powder electron diffraction experiments.

2.4.5. Texture analysis

By J. L. Lábár

The orientation distribution in a polycrystalline (nanocrystalline) TEM sample (used for powder electron diffraction) can either be random or a large fraction of grains can favour a special direction, *i.e.* the sample is textured. The texture can originate from the non-spherical shape of the particles (as in sedimentation geology or drop-drying of a suspension of nanoparticles on a TEM grid) or from energetic and/or kinetic conditions during nucleation and growth of grains in the formation of polycrystalline thin films on a substrate or, alternatively, the texture can be a result of mechanical deformation (as in drawing wires or rolling sheets of metals). Although the distribution of the preferred orientations can be very different, a few general types are frequently observed.

In the simplest case only one preferred-orientation vector characterizes the sample and the orientations of the grains are distributed arbitrarily around that direction. This situation is called *fibre texture* (single-axis texture). The most typical representatives of this texture class are sedimentation platy particles on a flat surface where the preferred-orientation vector is normal to the flat face of the particles, or a drawn metal wire where the preferred-orientation vector is directed along the wire axis. Another texture type frequently observed in the sedimentation of rod-shaped particles is described by the preferred-orientation vector being confined within a plane, but being arbitrarily oriented within this plane. Rolling of metal sheets results in other, more complex, but well characterized texture types: 'copper-type', 'brass-type' and 'S-type' (Mecking, 1985).

There are different ways to handle texture with electron diffraction. One approach is to collect the orientation information from individual nanograins in an automated area scan and reconstruct pole figures and inverse pole figures on a medium-sized population of grains (Rauch *et al.*, 2008). In principle, this is a single-crystal method analysing the information from an assembly of crystals. The Russian crystallography group developed the theory of arcs in oblique texture and used such textured patterns in structure analysis (Vainshtein, 1964; Vainshtein & Zvyagin, 1992). The *TexPat* software (Oleynikov & Hovmoller, 2004) was designed and effectively applied to determining unit-cell parameters and refining structure from oblique textured electron diffraction patterns. Tang *et al.* (1996) developed a method to determine the axis of texture and distribution of directions around that axis. The March–Dollase model (Dollase, 1986) for the description of pole densities was adapted for electron diffraction and used for the simulation of ring patterns (Li, 2010); however, no attempt was made to determine the phase fractions or textured fractions automatically.

A simplified automatic treatment of texture was implemented in the *ProcessDiffraction* software (Lábár, 2008, 2009). Partial texture is approximated by a linear combination of an ideally sharp fibre texture and a random distribution of components. Both the textured and the random components are treated as separately determined volume fractions during quantitative phase analysis (see Section 2.4.4). The advantage of the method is that the determination of the textured fraction is combined with simultaneous handling of a quasi-kinematic scattering by the Blackman approximation, and these two effects, which both modify the relative intensities, are treated simultaneously on a unified platform.

The application of the most general method for determining texture from powder electron diffraction patterns is restricted to the thinnest samples where kinematic scattering holds (Gemmi, Voltolini *et al.*, 2011). The method consists of recording a set of powder electron diffraction patterns at defined tilt steps of the two-axis goniometer, covering a considerable part of the solid-angle range usually used for recording pole figures. Azimuthal sections are integrated separately in 10° steps. The resulting large three-dimensional data set is fed into a variant of the Rietveld method called *MAUD* (Lutterotti *et al.*, 1997), which has built-in scattering factors for electrons. The orientation density function (ODF) is determined from the measured data by discretization of the orientation space. For texture fitting the *EWIMV* algorithm is used (Lutterotti *et al.*, 2004), which can be applied with irregular pole figure coverage and includes smoothing methods based on a concept of the tube projection. Pole figures from the smoothed

ODF were obtained for both sediment aggregates and evaporated thin films (Gemmi, Voltolini *et al.*, 2011).

2.4.6. Rietveld refinement with electron diffraction data

By T. E. Gorelik and U. Kolb

The Rietveld refinement method was initially developed for neutron diffraction data (Rietveld, 1967, 1969). It has now become a standard technique which is extensively used with neutron, laboratory X-ray and synchrotron diffraction data. A detailed description of the method can be found in Chapter 4.7.

Compared with the popularity of Rietveld refinement in X-ray and neutron powder diffraction, its application to powder electron diffraction data is very limited. So far, Rietveld refinement with electron diffraction data has only been done for nanocrystalline Al, α-MnS (Gemmi, Fischer *et al.*, 2011), hydroxyapatite (Song *et al.*, 2012), intermetallic AuFe (Luo *et al.*, 2011), TiO_2 (Weirich *et al.*, 2000; Tonejc *et al.*, 2002; Djerdj & Tonejc, 2005, 2006) and $MnFe_2O_4$ (Kim *et al.*, 2009). An example of a fit with powder electron diffraction data obtained by Rietveld refinement for hydroxyapatite is shown in Fig. 2.4.7.

Two major factors limit the application of Rietveld refinement to electron powder diffraction. First, electron powder diffraction data are collected from a sample volume far smaller than that used in an X-ray experiment. Therefore, the average statistics are poor compared with those of X-ray data. Nevertheless, electron powder diffraction data from a small sample area or thin films can give specific information which is difficult to obtain using other methods. Second, the presence of dynamical effects in the electron diffraction data hinders quantitative assessment of reflection intensities. Dynamical effects are strongest in zone-axis electron diffraction geometry, when many beams belonging to the same systematic rows are excited simultaneously. In powder electron diffraction crystals are randomly oriented towards the electron beam, thus making the fraction of zonal patterns low, thereby reducing the dynamical scattering in the data (see Section 2.4.2 for a more detailed discussion).

Within the limit of kinematical diffraction, the principle of Rietveld refinement is the same for electrons and X-rays, except the electron atomic scattering factors are different. The refinement procedure can thus be performed using existing programs if it is possible to input the scattering factors for electrons. Most of the reported Rietveld refinements on electron powder diffraction data have been performed using *FullProf* (Rodríguez-Carvajal, 1993); a refinement in *MAUD* (Lutterotti *et al.*, 1999) has also been reported (Gemmi, Voltolini *et al.*, 2011).

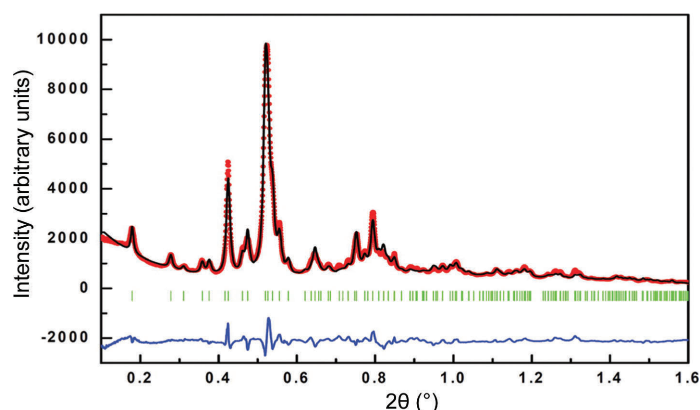

Figure 2.4.7
Rietveld analysis result with powder electron diffraction data of hydroxyapatite. Reproduced from Song *et al.* (2012) with permission from Oxford University Press.

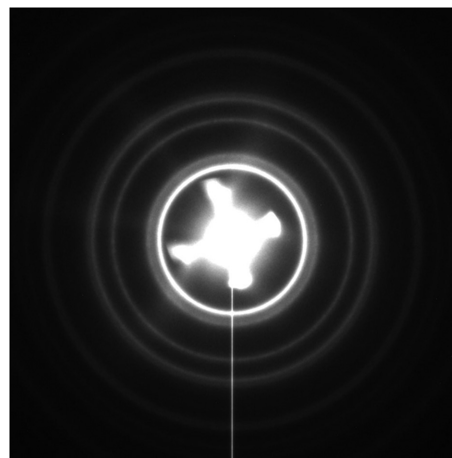

Figure 2.4.8
Powder electron diffraction pattern of nanocrystalline gold demonstrating non-symmetrical background features.

Electron powder diffraction patterns are recorded on an area detector. For a Rietveld refinement the two-dimensional diffraction patterns have to be integrated into one-dimensional profiles. The zero shift is treated as for the X-ray data integrated from a two-dimensional position-sensitive detector. Details about electron diffraction data processing and calibration are given in Section 2.4.3.4.

The background in electron powder patterns is a complex combination of inelastic scattering, scattering from the supporting film (when it is present) and other factors. For the Rietveld refinement procedure the background of a one-dimensional integrated profile is fitted by a polynomial function. If a supporting thin amorphous carbon film is used, the background can include broad rings, which after the one-dimensional integration can produce pronounced broad peaks. These peaks are difficult to subtract using a model based on a polynomial function; therefore, these intensities may hamper the powder diffraction profile matching (Kim *et al.*, 2009). In some cases, the background can even include radially non-symmetric features originating from the shape of the tip within the electron source (see Fig. 2.4.8); it can have blooming due to oversaturated CCD pixels, or streak shadows due to the fast transmission electron microscope beam-shutter movement. In these cases, a diffraction pattern from the adjacent ‘empty’ area of the sample can be acquired and subtracted from the diffraction pattern of the material prior to the integration into one dimension. This procedure allows elimination of some of the artifacts discussed above, which otherwise after the one-dimensional integration may be falsely interpreted as diffraction peaks, and are generally more difficult to fit.

Unit-cell parameters are mostly subject to the error due to the accuracy of the electron diffraction camera-length calibration. Although examples have been published showing 0.3% accuracy of the camera-length calibration, in most cases accuracy of about 2% can be achieved (Williams & Carter, 2009). The effective camera length depends on many instrumental parameters such as the convergence of the electron beam, the diffraction lens focus, the mechanical position of the sample within the objective lens, or the hysteresis of the electromagnetic lenses. Thus, while the ratio of the lattice parameters within one aligned diffraction pattern can be very precise, the absolute values might not be.

Atomic displacement parameters can be refined from electron powder diffraction data; however, the interpretation of the results can be manifold. For nanocrystalline materials, which have a relatively high surface-to-volume ratio, the surface effect can be enhanced compared with that of the bulk. Thus, the average atomic displacement factors can increase because of the high fraction of near-surface relaxed atoms. Consequently, the isotropic displacement parameter B resulting from the Rietveld refinement can be relatively high. Local heating (Reimer, 1984) during the electron illumination may also contribute to higher average displacement parameters. Finally, if the electron beam exceeds a material-dependent threshold acceleration voltage, it can cause knock-on damage (Williams & Carter, 2009) in both organic and inorganic materials. This is a dynamical process which can cause both material loss and rearrangement of atoms. The presence of defects resulting from the rearrangement of atoms may lead to an increase in the average displacement factors. Nevertheless, the refinement using polycrystalline anatase data showed the expected displacement parameters of 1.4 (1) $Å^2$ for Ti and 1.9 (2) $Å^2$ for oxygen (Weirich *et al.*, 2000). Of all the parameters used during Rietveld refinement, the displacement parameters and atomic coordinates are probably the most sensitive to a possible dynamical-scattering contribution in the data. It is noticeable that after the refinement of the anatase structure the atomic coordinates converged to reasonable positions: $[0, \frac{1}{4}, 0.1656\,(5)]$ for oxygen (Weirich *et al.*, 2000) compared with the previous range obtained in neutron diffraction studies of $[0, \frac{1}{4}, 0.16686\,(5)]$ (Burdett *et al.*, 1987) to $[0, \frac{1}{4}, 0.20806\,(5)]$ (Howard *et al.*, 1991).

The relative ratio of two components in a mixture can be determined using the Hill–Howard approach (Hill & Howard, 1987): the relative weight of a phase in a mixture of phases is proportional to the scaling factor of the phase given by the Rietveld refinement combined with the mass and the volume of the unit cell of the component. The relative content of a mixture of anatase and brookite was successfully determined from electron powder diffraction data (Djerdj & Tonejc, 2005, 2006).

For the modelling of the Bragg reflection shape the Pearson VII function can be used (Weirich *et al.*, 2000; Kim *et al.*, 2009), although recently the more popular pseudo-Voigt peak shape function has been used (Tonejc *et al.*, 2002; Djerdj & Tonejc, 2005, 2006) and provides a satisfactory fit between the experimental and calculated data.

The average crystalline domain size can be determined using line-broadening analysis. The measured intensity profile is a convolution of the physical line profile given by the sample with the instrumental profile broadening. When expressed in terms of the scattering angle θ, the width of the electron diffraction peaks is much smaller than that for X-rays. On the other hand, electrons generally have a smaller coherence length than X-rays. As a result, for the same material, the effective peak width for electron diffraction is larger than that for powder X-ray data (Song *et al.*, 2012). Because of this, it is sometimes difficult to separate the domain size and the instrumental contributions to the peak broadening. Therefore, the average domain size obtained after the refinement procedure should be cross-checked with the domain size determined from TEM images obtained, for instance, using the dark-field technique (Williams & Carter, 2009).

In electron diffraction various instrumental parameters can affect the peak width. The energy spread of the electrons causes additional broadening of diffracted spots. This effect can be partially reduced by energy filtering of the diffraction patterns (Kim *et al.*, 2009; Egerton, 2011). Finally, the electron diffraction

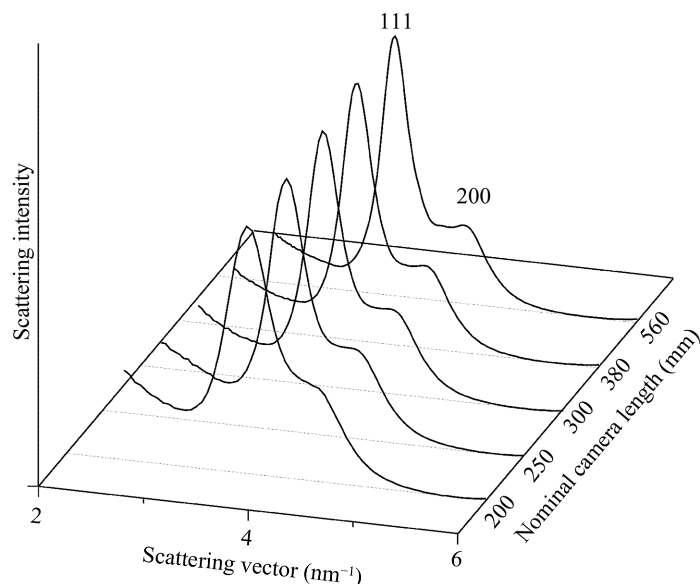

Figure 2.4.9
Electron powder diffraction profiles of gold nanoparticles (range 2–6 nm^{-1}) recorded at different electron diffraction camera lengths.

camera length must be large enough that the detector broadening is much smaller than the peak width, as demonstrated in Fig. 2.4.9: large values of the camera length ('zoomed in' diffraction patterns) result in thinner, better separated peaks.

Preferred orientation can be an issue for electron powder diffraction: when the powder material is supported on a thin film, the crystals tend to orient themselves with their most developed facet facing the support. As a result, the relative intensities of the diffracted peaks are modified (Kim *et al.*, 2009). Texture within nanocrystalline powders introduced by the sample preparation on a support for TEM can be analysed using electron powder diffraction patterns recorded at different tilt positions of the sample. Refinement of the preferred orientation of two different materials – nanocrystalline aluminium and α-MnS powders – showed that the aluminium particles tend to have strong preferred orientation due to their facet morphology, while α-MnS particles are randomly oriented (Gemmi, Fischer *et al.*, 2011).

Although dynamical effects are believed to be reduced for nanocrystalline materials and additionally reduced by data collection from non-oriented crystals, the dynamical component of the scattering cannot be neglected. For the dynamical correction using the two-beam approximation formalism of equation (2.4.12), the reader is referred to Section 2.4.2. For a range of electron-beam energies from 20 to 50 kV it has been shown that polycrystalline electron diffraction patterns of aluminium crystals smaller than 9 nm have a dynamical scattering component below 10% (Horstmann & Meyer, 1962). For polycrystalline $MnFe_2O_4$ with an average crystal size of 11 nm measured using a 120 kV electron beam, the ratio of the kinematical to dynamical contributions in the structure factor was about 1:1.5 (Kim *et al.*, 2009). The application of the small (less than 3%) correction for the dynamical component during Rietveld refinement of nanocrystalline intermetallic Au_3Fe_{1-x} improved the refined long-range order parameter of the alloy (Luo *et al.*, 2011).

In summary, the Rietveld refinement technique applied to electron powder diffraction data is a new area of research. It can be successfully carried out for small volumes of nanocrystalline materials, for which the small electron beam is an advantage. Results obtained from Rietveld analysis of electron powder

diffraction data of nanocrystalline materials are encouraging. The refinement for powders containing large crystal grains is problematic because of dynamical scattering present in the data. There are also uncertainties caused by instrumental effects. The dynamical effects can be accounted for using the Blackman formalism, while the influence of diverse instrumental parameters needs further systematic study.

2.4.7. The pair distribution function from electron diffraction data

By T. E. Gorelik and U. Kolb

An extensive description of pair distribution function (PDF) analysis covering data acquisition, reduction and interpretation can be found in Chapter 5.7. Here, only a short outline is presented, concentrating on aspects that are specific to PDFs obtained by electron diffraction.

Poorly crystalline and amorphous materials exhibit no long-range order and therefore show no pronounced Bragg peaks in diffraction patterns. Nevertheless, owing to defined bonding geometry, these materials do have a specific local arrangement of atoms, denoted as short-range order. The short-range order can be analysed using the PDF obtained from the total scattering profile. The PDF can provide general information about the degree of order, the character of local atomic packing and the size of the correlation domains. The total scattering function is collected over a wide range of reciprocal space and includes not only the Bragg reflections (if present), but also the diffuse scattering information between them (Egami & Billinge, 2003).

The PDF $G(r)$ represents the probability of finding a pair of atoms with an interatomic distance r, weighted by the scattering power of the individual atoms. After normalization and suitable corrections, the reduced scattering function $F(Q)$ is derived. [In the PDF analysis, the scattering vector Q, which is related to the scattering angle θ as $Q = (4\pi \sin\theta)/\lambda$ is used, instead of $S = \sin\theta/\lambda$.] The PDF can be calculated by the Fourier transformation of $F(Q)$ into direct space (Warren, 1990; Egami & Billinge, 2003; Farrow & Billinge, 2009).

Powder diffraction data for PDF analysis should be measured over a sufficiently large range of the scattering angle θ; therefore, neutron or synchrotron sources or laboratory X-ray data with a short-wavelength source (Mo or Ag anode) are used. Powder electron diffraction data, with their flexibility in electron diffraction camera length, short wavelength and nuclear scattering at large scattering angles, can also cover the desired large range of scattering angles and are therefore highly suitable for PDF analysis. In addition, atoms have a much larger scattering cross section for electrons than for X-rays or neutrons, allowing sufficient signal collection from very small volumes. Finally, electrons can be focused with lenses down to a few nanometres. All these reasons make electron diffraction analysis attractive for the study of the structure of nanovolumes. The electron PDF is therefore a powerful tool for the investigation of the structures of amorphous or poorly crystalline thin films, or for small sample volumes of inhomogeneous samples.

There are several practical issues to consider when collecting electron diffraction data for PDF analysis:

Energy filtering. Traditionally, electron diffraction data for PDF analysis are collected using energy filtering in order to exclude the inelastic scattering contribution. However, quantitative or semi-quantitative electron PDFs can be obtained without filtering (Abeykoon *et al.*, 2012).

Multiple scattering/dynamical effects. In order to keep the contribution of non-kinematic scattering low, the sample thickness and the nanoparticle size should be as small as possible. Generally, particles 10 nm and smaller should scatter kinematically, and this is the size range that benefits most from PDF analysis (Abeykoon *et al.*, 2012).

Powder average. Proper statistics are important for PDF analysis. In order to decrease measurement errors one can increase the illumination area on the sample (or the selected-area aperture in the case of SAED), collect several diffraction patterns from different areas and average them.

Scattering angle range. A large θ range is essential for PDF analysis. An electron diffraction experiment offers significant flexibility in selecting the scattering range through the adjustment of the electron diffraction camera length and illumination wavelengths. Additionally, in order to enhance the data quality, merging of different scattering ranges recorded in a set of diffraction patterns is possible (Petersen *et al.*, 2005).

An electron diffraction pattern is a combination of signals produced by *elastically* and *inelastically* scattered electrons. The inelastic component is a result of electron energy loss due to plasmon or inner-shell excitation, electron Compton or thermal diffuse scattering (Egerton, 2011). For crystalline materials with distinct Bragg peaks the inelastic scattering is not particularly critical, as it mainly contributes to the background in diffraction patterns and can be neglected when only the intensities of the Bragg peaks are analysed. For PDF analysis the total scattering profile is used; thus, the inelastic scattering, which can significantly modify the scattering profile, needs to be considered (Ishimaru, 2006). Two strategies are followed in this respect: (i) energy filtering of diffraction patterns, which is the more accurate approach but demands specific instrumentation, and (ii) subtraction of the background scattering taken from an area adjacent to the sample (*i.e.* from the supporting film), which assumes that the main inelastic scattering component originates from the support, and the contribution from the sample can be neglected (Cockayne, 2007). The validity of this approximation depends on the level of quantification intended in the particular study.

The PDF formalism presented above is based on the single-scattering approximation. Multiple scattering, which is much stronger in electron diffraction than for X-rays and neutrons, significantly affects the total scattering profile and therefore the PDF. The multiple-scattering effects can modify the peak positions in the PDF as well as the relative intensities of the peaks, the latter being more sensitive to multiple scattering (Anstis *et al.*, 1988). It has been shown that for amorphous materials, owing to the contribution of the multiple scattering, the total scattering profile depends on the thickness of the foil (Childs & Misell, 1972; Rez, 1983). Knowledge of the film thickness allows extraction of the single-scattering distribution. An improved agreement with the expected PDF was shown for hydrogenated amorphous silicon (Anstis *et al.*, 1988) and amorphous germanium (Ankele *et al.*, 2005) using the single-scattering profile.

Experimentally, it is difficult to determine the sample thickness along the incident-electron-beam direction. In this case, the thickness parameter employed in calculations can be varied, adjusting the amplitudes of the PDF. An estimate for the sample thickness is found when the optimal fit is obtained. Different input values of the thickness result in different principal gradients of the oscillations. Once a reasonable fit is found, the correct thickness is determined and the contribution of multiple scattering can be eliminated (Ankele *et al.*, 2005). This method was

applied to amorphous NiNb alloy, allowing an estimate of the foil thickness, and thereafter improved the fit to the PDF obtained from Ag-anode X-ray scattering experiments (Ankele *et al.*, 2005).

Alternatively, the wavelength dependence of the multiple-scattering term can be used. A set of diffraction patterns of a glassy carbon film was collected from the same sample (apparently having the same thickness) using different wavelengths (Petersen *et al.*, 2005). These patterns were then processed in order to retrieve the single-scattering profile of tetrahedral amorphous carbon, which showed an improved fit to the reduced scattering function obtained with neutrons (Petersen *et al.*, 2005). This method can be applied to materials for which significant multiple scattering is expected and the thickness of the foil cannot be determined *a priori*. For very thin films the contribution of the multiple scattering is very low and, therefore, often neglected.

The PDF of elemental materials arising from only one contributing atomic scattering function can be directly interpreted in terms of coordination numbers and allows conclusions to be drawn about the local structure. PDF analysis of amorphous silicon prepared by deposition showed the existence of voids in the structure (Moss & Graczyk, 1969) which anneal on progressive heating. PDF investigation of amorphous carbon films prepared by arc plasma deposition showed that the material mainly consists of tetrahedrally coordinated carbon rather than having a graphitic structure (McKenzie *et al.*, 1991).

For ZrNi and ZrCu metallic glasses, partial PDFs were obtained by reverse Monte Carlo simulation (McGreevy & Pusztai, 1988) and fitted to the experimentally obtained electron scattering data. The analysis of the polyhedral statistics showed that the average coordination number of Cu was 11, while for Ni it was less than 10 (Hirata *et al.*, 2007). Study of amorphous FeB alloys (Hirata *et al.*, 2006) and $Fe_{90}Zr_7B_3$ (Hirotsu *et al.*, 2003) by PDF analysis allowed detection of nanoscale phase separation resulting in the formation of a mixture of different clusters.

Nanocrystals can be efficiently analysed by electron PDF analysis, giving information complementary to TEM imaging. The electron PDF of detonation nanodiamonds (DND) was used to estimate the average domain size (Zhang, 2011). Studies of phase separation in AgCu alloys showed the complex behaviour of the material with variation of temperature (Chen & Zuo, 2007). In the first stage, the nanodomains of the two terminal phases (Ag- and Cu-rich) are built; in the second stage, dewetting of the thin film and formation of large Ag and Cu grains occur. A comparison of electron PDFs from nanocrystalline, partially ordered and amorphous parts of silica glasses (Kovács Kis *et al.*, 2006) allowed the estimation of the degree of order developed by changing the connectivity and orientation of the undistorted SiO_4 tetrahedra. Indirect detection of hydrogen atoms was performed from a modified distribution of atomic distances in soot samples using electron PDF analysis (Kis *et al.*, 2006).

With an increase in the particle size the deviations from the kinematical scattering become severe. Nevertheless, the electron PDF calculated for 100 nm Au crystals reproduced the simulated data quite well: the peak positions and relative amplitudes were not significantly modified (Abeykoon *et al.*, 2012).

2.4.8. Summary

Powder electron diffraction can be used for materials structural characterization, just as is routinely done using X-rays and neutrons. The specific characteristics of electron scattering result in both benefits and drawbacks to using electron diffraction data. Strong scattering of electrons allows collection of a sufficient signal from nanovolumes of material, thus offering the possibility of studying small amounts of material and thin films. The opportunity to couple the diffraction information with imaging gives the unique possibility of performing a structural study on the nanoscale in a controlled way. The strong interaction of electrons with matter leads to dynamical-scattering effects that result in deviation of the electron diffraction intensities from the kinematical model. Since the amount of the dynamical-scattering component in a powder sample is difficult to quantify, the quantitative use of electron diffraction intensity data is limited. For large crystals, the dynamical treatment of electron diffraction data is efficiently done in CBED analysis, providing exclusive information about the structure. For nanocrystalline or amorphous materials, an increasing number of sets of experimental data show that quantitative structure information can be obtained using electron powder diffraction. This encourages further applications of different kinds of electron diffraction data, giving new perspectives for the quantitative use of electron diffraction in general.

APPENDIX A2.4.1
Computer programs for electron powder diffraction

CHECKCELL is a graphical powder-pattern indexing helper and space-group-assignment program that links into the *CRYSFIRE* powder indexing suite. More information and the program are available at http://www.ccp14.ac.uk/tutorial/lmgp/achekcelld.htm.

CRYSFIRE is a powder-pattern indexing system for DOS/Windows for unit-cell parameter determination from powder data (free for academic use). More information and the program are available at http://www.ccp14.ac.uk/tutorial/crys/.

ELD is a commercial program for calibrating and integrating two-dimensional electron diffraction patterns. The program is commercially available from Calidris, Sweden. More information is available from http://www.calidris-em.com/eld.php.

Electron diffraction pattern atlas. The website of Professor Jean-Paul Morniroli (http://electron-diffraction.fr/) provides an atlas of electron diffraction patterns that can be used to identify the space group of a crystal from observation of a few typical PED and CBED zone-axis patterns.

FIT2D is a general-purpose image and diffraction processing program, designed for use with synchrotron data, that integrates pre-selected sections of either one-dimensional or two-dimensional data. Corrections for geometrical distortion and for nonlinearity of intensity are included. It is available both for the Windows operating system (and DOS window) and for Macintosh OSX. The program is freely available for academic users. More information and the program are available at http://www.esrf.eu/computing/scientific/FIT2D/.

JEMS is a popular suite of simulation routines for a variety of platforms, mainly used for simulating high-resolution TEM (HRTEM), CBED, PED and SAED patterns. Simulation of powder diffraction rings is also included. The student version is free of charge. A licence is available from the author: http://www.jems-saas.ch/.

PCED is a program for the simulation of polycrystalline electron diffraction patterns (Li, 2010). A licence file is needed to unlock the program for loading input data files. More information is available at http://www.unl.edu/ncmn-cfem/xzli/.

PDFgui and *PDFfit2* are programs for full-profile fitting of the atomic PDF derived from X-ray or neutron diffraction data. *PDFgui* is a graphical front end for the *PDFfit2* refinement program, with built-in graphical and structure-visualization capabilities. *PDFgui* is currently in beta release and it is distributed as part of the DiffPy library. More information and the program are available at http://www.diffpy.org.

Process Diffraction is designed for processing of SAED and NAED patterns. It includes quantitative determination of phase fractions and texture from ring patterns recorded from nanocrystalline thin films in TEM. More information and the program are available at http://www.energia.mta.hu/~labar/ProcDif.htm.

QPCED and *PCED* are Java-based software for digitization, processing, quantification and simulation of powder electron diffraction patterns. For information contact Dr X. Z. Li (xzli@unl.edu) or visit http://www.unl.edu/ncmn-cfem/xzli.

TexPat is a program for quantification of texture (preferred orientation) from a tilt series of ring patterns recorded from nanocrystalline thin films in TEM (Oleynikov & Hovmoller, 2004).

WebEMAPS is a suite of computer programs that can be obtained at http://cbed.matse.illinois.edu/software_emaps.html. The programs include functions for visualization of crystal structures, simulation of single-crystal diffraction patterns, dynamic electron diffraction simulation, and calculations of electron structure factors and lattice *d*-spacings.

WinPLOTR is a peak-search program for plotting powder diffraction patterns and can be used as a graphical user interface for several programs used frequently in powder diffraction data analysis (*e.g. FullProf*, *DicVOL*, *SuperCELL*). *WinPLOTR* has been developed to run on PCs with a 32-bit Microsoft Windows operating system. More information and the program are available at http://www.cdifx.univ-rennes1.fr/winplotr/readme.htm.

References

Abeykoon, M. C. D., Malliakas, C. D., Juhás, P., Bozin, E. S., Kanatzidis, M. G. & Billinge, S. J. L. (2012). *Quantitative nanostructure characterization using atomic pair distribution functions obtained from laboratory electron microscopes. Z. Kristallogr.* **227**, 248–256.

Ankele, J., Mayer, J., Lamparter, P. & Steeb, S. (2005). *Quantitative electron diffraction data of amorphous materials. Z. Naturforsch. A*, **60**, 459–468.

Anstis, G. R. Z., Liu, Z. & Lake, M. (1988). *Investigation of amorphous materials by electron diffraction – the effects of multiple scattering. Ultramicroscopy*, **26**, 65–69.

Baerlocher, C., Gramm, F., Massüger, L., McCusker, L. B., He, Z., Hovmöller, S. & Zou, X. (2007). *Structure of the polycrystalline zeolite catalyst IM-5 solved by enhanced charge flipping. Science*, **315**, 1113–1116.

Barna, Á. & Pécz, B. (1997). *Preparation techniques for transmission electron microscopy.* In *Handbook of Microscopy*, edited by S. Amelinckx, D. van Dyck, J. van Landuyt & G. van Tendeloo, Vol. 3, pp. 751–801. Weinheim: Wiley-VCH Verlag GmbH.

Blackman, M. (1939). *On the intensities of electron diffraction rings. Proc. R. Soc. London Ser. A*, **173**, 68–82.

Botton, G. (2007). *Analytical electron microscopy*. In *Science of Microscopy*, edited by P. Hawkes & J. C. H. Spence, pp. 273–405. New York: Springer.

Burdett, J. K. T., Hughbanks, T., Miller, G. J., Richardson, J. W. & Smith, J. V. (1987). *Structural–electronic relationships in inorganic solids: powder neutron diffraction studies of the rutile and anatase polymorphs of titanium dioxide at 15 and 295 K. J. Am. Chem. Soc.* **109**, 3639–3646.

Chen, H. & Zuo, J. M. (2007). *Structure and phase separation of Ag–Cu alloy thin films. Acta Mater.* **55**, 1617–1628.

Childs, P. A. & Misell, D. L. (1972). *Some aspects of elastic plural scattering of electrons by atoms. J. Phys. D Appl. Phys.* **5**, 2095.

Cockayne, D. J. H. (2007). *The study of nanovolumes of amorphous materials using electron scattering. Annu. Rev. Mater. Res.* **37**, 159–187.

Cockayne, D. J. H. & McKenzie, D. R. (1988). *Electron diffraction analysis of polycrystalline and amorphous thin films. Acta Cryst.* A**44**, 870–878.

Cowley, J. M. (1992). *Electron Diffraction Techniques*. International Union of Crystallography Monographs on Crystallography. Oxford: IUCr/Oxford University Press.

Cowley, J. M. (1995). *Diffraction Physics*. Amsterdam: Elsevier Science BV.

Cowley, J. M. (1999). *Electron nanodiffraction. Microsc. Res. Tech.* **46**, 75–97.

Cowley, J. M. & Hewat, A. W. (2004). *Powder and related techniques: electron and neutron techniques*. *International Tables for Crystallography* Vol. C, pp. 80–83. Dordrecht: Kluwer Academic Publishers.

Djerdj, I. & Tonejc, A. M. (2005). *Transmission electron microscopy studies of nanostructured TiO_2 films on various substrates. Vacuum*, **80**, 371–378.

Djerdj, I. & Tonejc, A. M. (2006). *Structural investigations of nanocrystalline TiO_2 samples. J. Alloys Compd.* **413**, 159–174.

Dollase, W. A. (1986). *Correction of intensities for preferred orientation in powder diffractometry: application of the March model. J. Appl. Cryst.* **19**, 267–272.

Egami, T. & Billinge, S. J. L. (2003). *Underneath the Bragg Peaks: Structural Analysis of Complex Materials*. Oxford: Pergamon.

Egerton, R. F. (2011). *Electron Energy-Loss Spectroscopy in the Electron Microscope*. New York: Plenum Press.

Elsayedali, H. E. & Herman, J. W. (1990). *Ultrahigh vacuum picosecond laser-driven electron diffraction system. Rev. Sci. Instrum.* **61**, 1636–1647.

Faber, J. & Fawcett, T. (2002). *The Powder Diffraction File: present and future. Acta Cryst.* B**58**, 325–332.

Farrow, C. L. & Billinge, S. J. L. (2009). *Relationship between the atomic pair distribution function and small-angle scattering: implications for modeling of nanoparticles. Acta Cryst.* A**65**, 232–239.

Gammer, C. C., Mangler, C., Rentenberger, C. & Karnthaler, H. P. (2010). *Quantitative local profile analysis of nanomaterials by electron diffraction. Scr. Mater.* **63**, 312–315.

Gemmi, M. J., Fischer, J., Merlini, M., Poli, S., Fumagalli, P., Mugnaioli, E. & Kolb, U. (2011). *A new hydrous Al-bearing pyroxene as a water carrier in subduction zones. Earth Planet. Sci. Lett.* **310**, 422–428.

Gemmi, M., Voltolini, M., Ferretti, A. M. & Ponti, A. (2011). *Quantitative texture analysis from powder-like electron diffraction data. J. Appl. Cryst.* **44**, 454–461.

Gemmi, M., Zou, X. D., Hovmöller, S., Migliori, A., Vennström, M. & Andersson, Y. (2003). *Structure of Ti_2P solved by three-dimensional electron diffraction data collected with the precession technique and high-resolution electron microscopy. Acta Cryst.* A**59**, 117–126.

Gjonnes, K., Cheng, Y., Berg, B. S. & Hansen, V. (1998). *Corrections for multiple scattering in integrated electron diffraction intensities. Application to determination of structure factors in the [001] projection of Al_mFe. Acta Cryst.* A**54**, 102–119.

Gorelik, T., Matveeva, G., Kolb, U., Schleuss, T., Kilbinger, A. F. M., van de Streek, J., Bohled, A. & Brunklaus, G. (2010). *H-bonding schemes of di- and tri-p-benzamides assessed by a combination of electron diffraction, X-ray powder diffraction and solid-state NMR. CrystEngComm*, **12**, 1824–1832.

Gramm, F. C., Baerlocher, C., McCusker, L. B., Warrender, S. J., Wright, P. A., Han, B., Hong, S. B., Liu, Z., Ohsuna, T. & Terasaki, O. (2006). *Complex zeolite structure solved by combining powder diffraction and electron microscopy. Nature*, **444**, 79–81.

Haider, M. H., Rose, H., Uhlemann, S., Schwan, E., Kabius, B. & Urban, K. (1998). *A spherical-aberration-corrected 200 kV transmission electron microscope. Ultramicroscopy*, **75**, 53–60.

Henderson, R. (1995). *The potential and limitations of neutrons, electrons and X-rays for atomic resolution microscopy of unstained biological molecules. Q. Rev. Biophys.* **28**, 171–193.

Hill, R. J. & Howard, C. J. (1987). *Quantitative phase analysis from neutron powder diffraction data using the Rietveld method. J. Appl. Cryst.* **20**, 467–474.

Hirata, A., Hirotsu, Y., Ohkubo, T., Hanada, T. & Bengus, V. Z. (2006). *Compositional dependence of local atomic structures in amorphous $Fe_{100-x}B_x$ (x = 14, 17, 20) alloys studied by electron diffraction and high-resolution electron microscopy. Phys. Rev. B*, **74**, 214206.

Hirata, A. T., Morino, T., Hirotsu, Y., Itoh, K. & Fukunaga, T. (2007). *Local atomic structure analysis of Zr-Ni and Zr-Cu metallic glasses using electron diffraction. Mater. Trans.* **48**, 1299–1303.

Hirotsu, Y. T., Ohkubo, T., Bae, I.-T. & Ishimaru, M. (2003). *Electron diffraction structure analysis for amorphous materials. Mater. Chem. Phys.* **81**, 360–363.

Horstmann, M. & Meyer, G. (1962). *Messung der elastischen Elektronenbeugungsintensitäten polykristalliner Aluminium-Schichten. Acta Cryst.* **15**, 271–281.

Hovmoller, S., Zou, X. & Weirich, T. E. (2002). *Crystal structure determination from EM images and electron diffraction patterns. Adv. Imaging Electron Phys.* **123**, 257–289.

Howard, C. J., Sabine, T. M. & Dickson, F. (1991). *Structural and thermal parameters for rutile and anatase. Acta Cryst.* B**47**, 462–468.

Ichimiya, A. & Cohen, P. I. (2004). *Reflection High-Energy Electron Diffraction*. Cambridge University Press.

International Tables for Crystallography (2004). Volume C, *Mathematical, Physical and Chemical Tables*, edited by E. Prince. Dordrecht: Kluwer Academic Publishers.

Ishimaru, M. (2006). *Electron-beam radial distribution analysis of irradiation-induced amorphous SiC. Nucl. Instrum. Methods Phys. Res. Sect. B*, **250**, 309–314.

Ishimaru, M., Bae, I.-T., Hirotsu, Y., Matsumura, S. & Sickafus, K. E. (2002). *Structural relaxation of amorphous silicon carbide. Phys. Rev. Lett.* **89**, 055502.

Jansen, J., Tang, D., Zandbergen, H. W. & Schenk, H. (1998). *MSLS, a least-squares procedure for accurate crystal structure refinement from dynamical electron diffraction patterns. Acta Cryst.* A**54**, 91–101.

Kim, J. G., Seo, J. W., Cheon, J. & Kim, Y. J. (2009). *Rietveld analysis of nano-crystalline $MnFe_2O_4$ with electron powder diffraction. Bull. Korean Chem. Soc.* **30**, 183–187.

Kis, V. K. M., Posfai, M. & Labar, J. (2006). *Nanostructure of atmospheric soot particles. Atmos. Environ.* **40**, 5533–5542.

Kolb, U. K., Büscher, K., Helm, C. A., Lindner, A., Thünemann, A. F., Menzel, M., Higuchi, M. & Kurth, D. G. (2006). *The solid-state architecture of a metallosupramolecular polyelectrolyte. Proc. Natl Acad. Sci. USA*, **103**, 10202–10206.

Kovács Kis, V., Dódony, I. & Lábár, J. L. (2006). *Amorphous and partly ordered structures in SiO_2 rich volcanic glasses. An ED study. Eur. J. Mineral.* **18**, 745–752.

Lábár, J. L. (2006). *Phase identification by combining local composition from EDX with information from diffraction database.* In *Electron Crystallography*, edited by T. E. Weirich, J. L. Lábár & X. Zou, Nato Science Series II, Vol. 211, pp. 207–218. Dordrecht: Springer.

Lábár, J. L. (2008). *Electron diffraction based analysis of phase fractions and texture in nanocrystalline thin films, part I: principles. Microsc. Microanal.* **14**, 287–295.

Lábár, J. L. (2009). *Electron diffraction based analysis of phase fractions and texture in nanocrystalline thin films, part II: implementation. Microsc. Microanal.* **15**, 20–29.

Lábár, J. L. & Adamik, M. (2001). *ProcessDiffraction V1.2: new possibilities in manipulating electron diffraction ring patterns. Microsc. Microanal.* **7** (Suppl. 2), 372–373.

Lábár, J. L. M., Adamik, M., Barna, B. P., Czigány, Z., Fogarassy, Z., Horváth, Z. E., Geszti, O., Misják, F., Morgiel, J., Radnóczi, G., Sáfrán, G., Székely, L. & Szüts, T. (2012). *Electron diffraction based analysis of phase fractions and texture in nanocrystalline thin films, part III: application examples. Microsc. Microanal.* **18**, 406–420.

Lábár, J. L. & Egerton, R. (1999). *Special issue on ion beam techniques. Micron*, **30**, 195–196.

Li, X. Z. (2010). *PCED2.0 – a computer program for the simulation of polycrystalline electron diffraction pattern. Ultramicroscopy*, **110**, 297–304.

Luo, Z., Vasquez, Y., Bondi, J. F. & Schaak, R. E. (2011). *Pawley and Rietveld refinements using electron diffraction from $L1_2$-type intermetallic Au_3Fe_{1-x} nanocrystals during their in-situ order–disorder transition. Ultramicroscopy*, **111**, 1295–1304.

Lutterotti, L. D., Chateigner, D., Ferrari, S. & Ricote, J. (2004). *Texture, residual stress and structural analysis of thin films using a combined X-ray analysis. Thin Solid Films*, **450**, 34–41.

Lutterotti, L., Matthies, S. & Wenk, H. R. (1999). *MAUD: a friendly Java program for Material Analysis Using Diffraction. IUCr CPD Newsletters*, **21**, May 1999. http://www.mx.iucr.org/iucr-top/comm/cpd/Newsletters/no21may1999/art17/art17.htm.

Lutterotti, L. S., Matthies, S., Wenk, H.-R., Schultz, A. S. & Richardson, J. W. Jr (1997). *Combined texture and structure analysis of deformed limestone from time-of-flight neutron diffraction spectra. J. Appl. Phys.* **81**, 594–600.

McCusker, L. B. & Baerlocher, C. (2009). *Using electron microscopy to complement X-ray powder diffraction data to solve complex crystal structures. Chem. Commun.* pp. 1439–1451.

McGreevy, R. L. & Pusztai, L. (1988). *Reverse Monte Carlo simulation: a new technique for the determination of disordered structures. Mol. Simul.* **1**, 359–367.

McKenzie, D. R., Muller, D., Pailthorpe, B. A., Wang, Z. H., Kravtchinskaia, E., Segal, D., Lukins, P. B., Swift, P. D., Martin, P. J., Amaratunga, G., Gaskell, P. H. & Saeed, A. (1991). *Properties of tetrahedral amorphous carbon prepared by vacuum arc deposition. Diamond Relat. Mater.* **1**, 51–59.

Mecking, H. (1985). *Textures of metals*. In *Preferred Orientation in Deformed Metals and Rocks: An Introduction to Modern Texture Analysis*, edited by H.-R. Wenk, pp. 267–306. Orlando/London: Academic Press Inc.

Moeck, P. & Fraundorf, P. (2007). *Structural fingerprinting in the transmission electron microscope: overview and opportunities to implement enhanced strategies for nanocrystal identification. Z. Kristallogr.* **222**, 634–645.

Moeck, P. & Rouvimov, S. (2010). *Precession electron diffraction and its advantages for structural fingerprinting in the transmission electron microscope. Z. Kristallogr.* **225**, 110–124.

Moss, S. C. & Graczyk, J. F. (1969). *Evidence of voids within the as-deposited structure of glassy silicon. Phys. Rev. Lett.* **23**, 1167–1171.

Mugnaioli, E., Andrusenko, I., Schüler, T., Loges, N., Dinnebier, R. E., Panthöfer, M., Tremel, W. & Kolb, U. (2012). *Ab initio structure determination of vaterite by automated electron diffraction. Angew. Chem.* **51**, 7041–7045.

Nelder, J. A. & Mead, R. (1965). *A simplex method for function minimization. Comput. J.* **7**, 308–313.

Oleynikov, P. & Hovmoller, S. (2004). *TexPat – a program for quantitative analysis of oblique texture electron diffraction patterns. Z. Kristallogr.* **219**, 12–19.

Oleynikov, P. & Hovmoller, S. (2007). *Precession electron diffraction: observed and calculated intensities. Ultramicroscopy*, **107**, 523–533.

Orloff, J., Swanson, L. & Utlaut, M. (2002). *High Resolution Focused Ion Beams: FIB and Applications*. New York: Springer.

Own, C. S., Marks, L. D. & Sinkler, W. (2006). *Precession electron diffraction 1: multislice simulation. Acta Cryst.* A**62**, 434–443.

Őzdöl, V. B., Srot, V. & van Aken, P. A. (2012). *Sample preparation for transmission electron microscopy.* In *Handbook of Nanoscopy*, edited by G. Van Tendeloo, D. Van Dyck & S. J. Pennycook. Weinheim: Wiley.

Peng, L. M., Dudarev, S. L. & Whelan, M. J. (2004). *High-Energy Electron Diffraction and Microscopy*. USA: Oxford University Press.

Petersen, T. C., McBride, W., McCulloch, D. G., Snook, I. K. & Yarovsky, I. (2005). *Refinements in the collection of energy filtered diffraction patterns from disordered materials. Ultramicroscopy*, **103**, 275–283.

Rauch, E. F., Váron, M., Portillo, J., Bultreys, D., Maniette, Y. & Nicolopoulos, S. (2008). *Automatic crystal orientation and phase mapping in TEM by precession diffraction. Microsc. Anal.* **22**, S5–S8.

Reimer, L. (1984). *Transmission Electron Microscopy – Physics of Image Formation and Microanalysis*. Heidelberg: Springer-Verlag.

Reimer, L. & Kohl, H. (2008). *Transmission Electron Microscopy: Physics of Image Formation*. New York: Springer.

Rez, P. (1983). *A transport-equation theory of beam spreading in the electron microscope. Ultramicroscopy*, **12**, 29–38.

Rietveld, H. M. (1967). *Line profiles of neutron powder-diffraction peaks for structure refinement. Acta Cryst.* **22**, 151–152.

Rietveld, H. M. (1969). *A profile refinement method for nuclear and magnetic structures. J. Appl. Cryst.* **2**, 65–71.

Rodríguez-Carvajal, J. (1993). *Recent advances in magnetic structure determination by neutron powder diffraction. Physica B*, **192**, 55–69.

Rose, H. & Krahl, D. (1995). *Electron optics of imaging energy filters.* In *Energy-Filtering Transmission Electron Microscopy*, edited by L. Reimer, pp. 43–149. Berlin: Springer.

Saunders, M., Bird, D. M., Zaluzec, N. J., Burgess, W. G., Preston, A. R. & Humphreys, C. J. (1995). *Measurement of low-order structure factors for silicon from zone-axis CBED patterns. Ultramicroscopy*, **60**, 311–323.

Siwick, B. J., Dwyer, J. R., Jordan, R. E. & Miller, R. J. D. (2003). *An atomic-level view of melting using femtosecond electron diffraction. Science*, **302**, 1382–1385.

Song, K. Y. J., Kim, Y.-J., Kim, Y.-I. & Kim, J.-G. (2012). *Application of theta-scan precession electron diffraction to structure analysis of hydroxyapatite nanopowder. J. Electron Microsc.* **61**, 9–15.

Sun, J., Bonneau, C., Cantín, A., Corma, A., Díaz-Cabañas, M. J., Moliner, M., Zhang, D., Li, M. & Zou, X. (2009). *The ITQ-37 mesoporous chiral zeolite. Nature*, **458**, 1154–1157.

Tang, L., Feng, Y. C., Lee, L.-L. & Laughlin, D. E. (1996). *Electron diffraction patterns of fibrous and lamellar textured polycrystalline thin films. II. Applications. J. Appl. Cryst.* **29**, 419–426.

Tonejc, A. M., Djerdj, I. & Tonejc, A. (2002). *An analysis of evolution of grain size-lattice parameters dependence in nanocrystalline* TiO_2 *anatase. Mater. Sci. Eng. C*, **19**, 85–89.

Tsuda, K., Ogata, Y., Takagi, K., Hashimoto, T. & Tanaka, M. (2002). *Refinement of crystal structural parameters and charge density using convergent-beam electron diffraction – the rhombohedral phase of* $LaCrO_3$*. Acta Cryst.* A**58**, 514–525.

Tsuda, K. & Tanaka, M. (1999). *Refinement of crystal structural parameters using two-dimensional energy-filtered CBED patterns. Acta Cryst.* A**55**, 939–954.

Turner, P. S. & Cowley, J. M. (1969). *The effects of N-beam dynamical diffraction on electron diffraction intensities from polycrystalline materials. Acta Cryst.* A**25**, 475–481.

Ungár, T., Gubicza, J., Ribárik, G. & Borbély, A. (2001). *Crystallite size distribution and dislocation structure determined by diffraction profile analysis: principles and practical application to cubic and hexagonal crystals. J. Appl. Cryst.* **34**, 298–310.

Vainshtein, B. K. (1964). *Structure Analysis by Electron Diffraction*. Oxford: Pergamon Press.

Vainshtein, B. K., Zvyagin, B. B. & Avilov, A. S. (1992). *Electron diffraction structure analysis.* In *Electron Diffraction Techniques*, Vol. 1, edited by J. M. Cowley, pp. 216–312. Oxford University Press.

Vincent, R. & Exelby, D. R. (1991). *Structure of metastable Al–Ge phases determined from HOLZ Patterson transforms. Philos. Mag. Lett.* **63**, 31–38.

Vincent, R. & Midgley, P. A. (1994). *Double conical beam-rocking system for measurement of integrated electron diffraction intensities. Ultramicroscopy*, **53**, 271–282.

Warren, B. E. (1990). *X-ray Diffraction*. New York: Dover Publications.

Weickenmeier, A. & Kohl, H. (1991). *Computation of absorptive form factors for high-energy electron diffraction. Acta Cryst.* A**47**, 590–597.

Weirich, T. E. M., Winterer, M., Seifried, S., Hahn, H. & Fuess, H. (2000). *Rietveld analysis of electron powder diffraction data from nanocrystalline anatase,* TiO_2*. Ultramicroscopy*, **81**, 263–270.

Williams, D. B. & Carter, C. B. (2009). *Transmission Electron Microscopy: a Textbook for Materials Science*. New York: Springer.

Wu, J. S. K., Leinenweber, K., Spence, J. C. H. & O'Keeffe, M. (2006). *Ab initio phasing of X-ray powder diffraction patterns by charge flipping. Nat. Mater.* **5**, 647–652.

Zhang, J. (2011). *Atomic structures of carbon nanomaterials studied by coherent electron diffraction.* PhD thesis, University of Illinois, USA.

Zhuang, J. L. K., Lommel, K., Ceglarek, D., Andrusenko, I., Kolb, U., Maracke, S., Sazama, U., Fröba, M. & Terfort, A. (2011). *Synthesis of a new copper-azobenzene dicarboxylate framework in the form of hierarchical bulk solids and thin films without and with patterning. Chem. Mater.* **23**, 5366–5374.

Zuo, J. M. (1993). *New method of Bravais lattice determination. Ultramicroscopy*, **52**, 459–464.

Zuo, J. M. (2000). *Electron detection characteristics of a slow-scan CCD camera, imaging plates and film, and electron image restoration. Microsc. Res. Tech.* **49**, 245–268.

Zuo, J. M. (2004). *Measurements of electron densities in solids: a real-space view of electronic structure and bonding in inorganic crystals. Rep. Prog. Phys.* **67**, 2053–2103.

Zuo, J. M., Gao, M., Tao, J., Li, B. Q., Twesten, R. & Petrov, I. (2004). *Coherent nano-area electron diffraction. Microsc. Res. Tech.* **64**, 347–355.

Zuo, J. M., Kim, M. & Holmestad, R. (1998). *A new approach to lattice parameter measurements using dynamic electron diffraction and pattern matching. J. Electron Microsc.* **47**, 121–127.

Zuo, J. M. & Spence, J. C. H. (1991). *Automated structure factor refinement from convergent-beam patterns. Ultramicroscopy*, **35**, 185–196.

Zuo, J. M. & Spence, J. C. H. (2017). *Advanced Transmission Electron Microscopy: Imaging and Diffraction in Nanoscience*. New York: Springer.